Infilling abandoned deltaic channels through tidal sedimentation: a case study from the Huanghe (Yellow River) delta, China

Carlson, B. N.[1], Nittrouer, J. A.[1], Moodie, A. J.[1], Kineke, G. C.[2], Kumpf, L.L.[2] , Ma, H.[1], Parsons, D.[3]

[1] Department of Earth, Environmental and Planetary Sciences, Rice University, Houston, Texas, USA.
[2] Earth and Environmental Sciences, Boston College, Chestnut Hill, Massachusetts, USA.
[3]Energy and Environment and Institute, University of Hull, Hull, UK

Corresponding author: Brandee Carlson (bc15@rice.edu)

Key Points:

- Field observations document exclusively marine-derived sediment delivered by tides accumulating within an abandoned distributary channel
- A simple numerical model informed by field measurements captures sediment concentration, distribution, and aggradation rates for the abandoned channel
- The shallow stratigraphy of an abandoned distributary channel displays a transition from an active channel to a mudflat, which is actively aggrading ~2 cm/yr

Abstract

Upon avulsion, abandoned deltaic distributary channels receives water and sediment delivered by a tie channel, overbank flow, and by tidal inundation from the receiving basin. The transport and deposition of sediment arising from this latter input have important impacts on delta development, yet are not well-constrained from field observations or numerical models. Herein, the Huanghe (Yellow River) delta of China is used as a case study to evaluate how marine-sourced sediment impacts abandoned channel morphology. For this system, artificial deltaic avulsions occur approximately decadally; the abandoned channels are inundated by tides, and deposition of sediment transforms the channel and adjacent lobe into a mudflat. Field data were collected from a channel abandoned twenty years ago, and included cores that penetrated the tidally deposited mud and antecedent fluvial channel sediment, topography and bathymetry surveys, and detailed time-series monitoring of hydrodynamic conditions within the tidal channel and adjacent mudflat. These data are used to validate a model that constrains material exchange between the channel and flat. The thickness of the marine-sourced mud differs spatially by an order of magnitude, and is primarily impacted by antecedent channel topography, rather than spatial variability in mud deposition, as has been observed in other mudflat environments. The system is nearing its limit of fill potential, which is set by the spring tide water elevation. As this elevation is below antecedent levees, assuming stationary sea level, the abandoned channel will remain a topographic low on the delta landscape and is therefore susceptible to reoccupation with future avulsions.

1 Introduction

An avulsion is the rapid abandonment of an active fluvial channel in favor of a new course [*Slingerland and Smith*, 2004], typically arising as sediment aggrades the channel bed more rapidly than its levees, thereby reducing cross-sectional flow area and elevating the channel relative to its surrounding floodplain [*Mackey and Bridge*, 1995; *Mohrig et al.*, 2000; *Hajek and Wolinsky*, 2012]. An avulsion usually occurs during a flood event, and is facilitated by a levee crevasse that conveys water from the main channel to the floodplain, which may create a new channel or find an antecedent channel that provides enhanced flow capacity [*Slingerland and Smith*, 2004]. Typically, a tie channel maintains a connection between the primary and abandoned channels, which, in addition to overbank flows of sediment-laden water during floods, maintains input of fresh water and fluvial sediment to the abandoned channel [*Rowland et* *al.*, 2005; *Toonen et al.*, 2012; *Gray et al.*, 2016]. As a result, it is possible to slowly fill abandoned channels with sediment over time [*Toonen et al.*, 2012; *Gray et al.*, 2016].

For most lowland fluvial systems, regional channel avulsions arise over timescales of 10^2–10^3 yrs. These events are unpredictable and rapid, so it is difficult to monitor occurrences in real-time [*Zinger et al.*, 2011]. Previous studies have utilized physical experiments [*Reitz et al.*, 2010], meander-scale avulsions in modern fluvial systems [*Smith et al.*, 1989; *Aslan and Autin*, 1999; *Aalto et al.*, 2008; *Toonen et al.*, 2012; *Gray et al.*, 2016], and ancient fluvial deposits preserved and exposed in rock outcrops [*Mohrig et al.*, 2000; *Chamberlin and Hajek*, 2015] to gain insights about avulsion processes. For example, data from experiments and rock strata studies have the unique advantage of documenting sediment variability arising due to multiple avulsion events, whereby vertically stacked, multistory channel sand bodies separated by overbank (mud) deposits indicate reoccupation of antecedent channels. It is proposed that as a consequence of incomplete filling, abandoned channels are rendered topographic lows and remain as preferential flow paths, susceptible to reoccupation with subsequent avulsions [*Mohrig et al.*, 2000; *Chamberlin and Hajek*, 2015].

The avulsion cycle and infilling of *deltaic distributary* channels, on the other hand, has received less attention. Deltaic avulsions are important as they relocate the fluvial depocenter and generate new lobes, thereby impacting the development of subaerial coastal landscape [*Kim et al.*, 2009; *Roberts, H.,* 1997]. Abandoned deltaic channels, present on low-relief deltas, maintain similarities to their fluvial counterparts insofar as they may serve as preferential pathways for future avulsions [*Reitz et al.*, 2010]. Yet, delta distributary channels are unique because they are impacted by waves and tides of the receiving basin, which rework and disperse sediment, eroding deltaic lobes [*Nienhuis et al.*, 2013]. For coastlines where the tidal range is large relative to typical wave heights, channel lobes may be transformed into mudflat — that is, sediment deposits that are periodically exposed and inundated during low and high tides. The surface morphology of mudflats evolves by spatiotemporal variation in flow velocity, and sediment transport and deposition patterns, arising with tidal asymmetries (discrepancy in flood/ebb flow velocity [*Friedrichs*, 2011; *Le Hir et al.*, 2000; *Mariotti and Fagherazzi*, 2012]), and temporal offset of the various phases of the tidal constituents [*Hoitink et al.*, 2003].

There is a limited understanding for the morphological development of a fluvial-deltaic lobe and associated channel upon abandonment by avulsion. The Huanghe (Yellow River) delta of China offers an intriguing study site: multiple abandoned lobes persist across the delta as a consequence of major channel avulsions occurring on a decadal timescale, largely due to engineered diversions (Fig. 1). The long-term outcome is that these former channels and lobes are transformed into mudflats; however, this process, as related to the impacts of waves and tides, remains unconstrained. For mudflats, flood tides route sediment-laden water from a tidal channel over the adjacent flat: water velocity in the tidal channel exceeds that of the open mudflat, and so the dominant direction of particles is directed toward the mudflat during flood tide. Deposition occurs during slack high water, when water velocity is sufficiently low for settling of fine sediment [*Mariotti and Fagherazzi*, 2012; *Mariotti and Fagherazzi*, 2011; *Friedrichs*, 2011; *Van Maren and Winterwerp*, 2013]. A scour lag – defined as the excess shear stress required to entrain fine (cohesive) particles relative to the shear stress required to keep those particles in suspension – combined with lower shear stress over the mudflat during ebb tide, prevents remobilization of deposited materials and facilitates sediment accumulation [*Ridderinkhof et al.*, 2000].

Herein, the infilling of a fluvial-deltaic channel abandoned after an avulsion, and the conversion of this channel into a mudflat, is assessed by evaluating the relative role of tides and waves for both fair weather and seasonal storm conditions. Field data are sourced from the abandoned Qingshuigou lobe of the Huanghe delta, which was active from 1976–1996. The Qingshuigou lobe was abandoned through engineering practices that completely cutoff upstream water and sediment supply, therefore the role of tides and waves for sediment delivery can be isolated from other complicating factors, such as fluvial and estuarine processes. Here, annealing of this distributary channel is considered in regard to the propensity for a channel to completely anneal, or persist as a topographic low on the fluvial-deltaic landscape, and therefore remain a possible site of fluvial channel reoccupation.

2 Regional Setting

Sourced from the Tibetan Plateau, the Huanghe traverses the North China Plain and debouches into the Bohai Sea where it builds the Huanghe delta [*Zhang et al.*, 1990]. High sediment loads of the Huanghe lead to enhanced morphodynamics relative to most other deltaic systems. For example, approximately every decade the Huanghe abandons a deltaic lobe to construct a new one through both natural and engineered avulsions [*Van Gelder et al.*, 1994; *Ganti et al.*, 2014b].

Hence, the delta is a composite of numerous lobes that have developed over the past century. Interestingly, the Huanghe maintains a single-channel lobe, i.e., there are no major natural bifurcations of the primary channel approaching its receiving basin.

The Bohai Sea influences the Huanghe delta lobes in several ways. Astronomical tides are mixed semi-diurnal, and microtidal to mesotidal, with a range of 0.6-0.8 m near the river mouth, and 1.5 – 2 m in the north Bohai Gulf and to the south in Laizhou Bay [*Zhang et al.*, 1990]. Associated current velocity is 1 – 2 m/s [*Wang et al.*, 2010]. A seasonal wave climate also impacts sediment transport. During summer months, southerly winds produce small significant waves heights (0.3–0.7 m [*Wang et al., 2014]*), and during winter months, strong northeasterly winds from the East Asian Winter Monsoon (EAWM) generate significant wave heights exceeding 4 m [*Wang et al.*, 2014]. Hence, winter is an active period and seabed sediment resuspension in the Bohai Sea is common.

Most of the abandoned distributary channels of the Huanghe delta have been partially, if not entirely, filled with sediment (Fig. 1) [*Pang and Si*, 1979; *Van Gelder et al.*, 1994; *Saito et al.*, 2000; *Chu et al.*, 2006]. The particular lobe and channel that is the focus of this study is the Qingshuigou lobe (Figs. 1, 2). When the Qingshuigou lobe was active, the subaerial deposit rapidly prograded into the Bohai at a rate approaching 1 km/yr, [*Wright and Nittrouer*, 1995; *Chu et al.*, 2006]. Winter storms were highly effective at suspending sediment delivered to the delta front, and these storms redistributed sediment along the coastline via fluid-mud formation, and downslope by way of slope failures [*Wright and Nittrouer*, 1995]. In July of 1996, an engineered avulsion rerouted this distributary channel ~20 km to the northeast; in essence, this represents a *de facto* avulsion. As a consequence of the engineered design, there is no upstream input of sediment or riverine water to the abandoned channel. The bed resides at an elevation that renders it intertidal and thus subject to periodic inundation of water. Over the last twenty years, the fluvial channel has converted into a mudflat, which currently maintains one primary tidal channel (Fig. 2). The former levees of the Qingshuigou channel are presently situated up to 1.5 m above the high-high tide elevation, and so tidal flows are contained by this antecedent topography. As a consequence of little freshwater input (exception for atmospheric precipitation), and high evaporation potential in the summer months, the abandoned Qingshuigou lobe mudflat maintains high salinity; hence, the only vegetation to occupy the mudflat—*suaeda salsa*—tolerates hypersaline conditions.

3 Materials and Methods

Field observations and a modeling framework are presented in this section. The field survey was designed to capture the major driving factors and processes that result in sediment accumulation within the Qingshuigou abandoned channel. The topographic survey was conducted to constrain boundary conditions for not only the fluid flow and sediment transport regimes, but also the sedimentological and morphological impacts of tides and waves at the field site. Field observations inform a simplified model that captures the primary parameters necessary to predict sediment transport for an abandoned deltaic distributary channel filling with exclusively marine-derived sediment.

3.1 Topographic Survey

Elevation data were collected during summer field surveys of 2016 and 2017 (Fig. 2). In 2016, total station survey measurements were collected along transects oriented transverse to the abandoned channel, spaced 500 m apart. Along the transects, elevation data were collected by survey points that were located based on the local elevation variation: points were spaced approximately 10 m where it was relatively flat, and 1-5 m where topography change was evident (e.g., tidal channel banks, channel beds, etc.). Several elevation benchmarks located 2.6-3.2 km northeast of the most landward position of the survey were used to reference the survey data to the Huang Hai elevation datum [*Zhang et al.*, 2012]. In 2017, the abandoned channel was surveyed with real-time kinematic (RTK) differential GPS survey equipment. Transects were spaced 1 km apart, coinciding with transects collected in 2016. The total station data collected in 2016 have a horizontal error of 0.020–0.088 m and a vertical error of 0.020–0.047 m, which increases with distance from the benchmark (i.e., the error propagates seaward). The RTK data have a horizontal error of 0.001 m and a vertical error of 0.0015 m.

A bathymetric survey was conducted within the main tidal channel in 2016 using a single-beam echo sounder (Lowrance, HDS-7). Data were collected at ~10 m spacing, and the survey covered areas of the channel that were too deep to wade for the total station and the RTK GPS survey. These bathymetric data were also referenced to the Huang Hai elevation datum using a pressure transducer located at a known elevation in the tidal channel.

3.2 Sedimentological Data

During two campaigns (summer 2015 and 2016), a series of cores and pits were excavated within the abandoned channel. Seventeen six-meter-long vibracores were obtained from the abandoned channel mudflat during the 2015 campaign (Fig. 3). A depth of 6 m was chosen to ensure penetration into the sediments that comprised the antecedent channel, which maintained a thalweg depth of ~1–4 m [*Van Gelder et al.*, 1994; *Wang and Liang*, 2000]. Seven coring transects oriented transverse to the channel were spaced one kilometer apart in the downstream direction. Three cores were extracted per transect, located on the right bank, left bank, and channel center. Cores were opened with a circular disk saw, described, and imaged. Samples were collected every 0.05 m in silt and clay packages, and 0.2 m in the sand packages. In 2016, 45 pits were excavated to provide increased spatial resolution of the shallow stratigraphy. Five pits were dug per transect (established during the 2015 campaign, Fig. 3). Pits were dug to the water table (~ 50 cm), which was usually adequate to resolve the sand-mud contact, interpreted to be the fluvial-to-tidal sediment transition (see below). Pits were described, taking note of grain-size transitions (abrupt vs. gradual). Samples were collected from the pits at 10-cm intervals. Grain size data for the core and pit samples were obtained by laser particle diffraction analysis using a Malvern Mastersizer 2000.

3.3 Tidal Channel Observations

In summer 2017 and winter 2018, a suite of instruments were deployed within the tidal channel to continuously monitor water velocity and depth. A Lowell Tilt Current Meter (TCM-1), which contains a 3-axis accelerometer and 3-axis magnetometer for measuring instrument tilt and bearing, was used to measure flow velocity. The instrument collected measurements at one-minute intervals and the resulting orientation data was converted to current velocity (considered the average value over the of the 75-cm-long instrument). Water depth in the primary tidal channel was measured using an Onset HOBO pressure transducer (PT3) logging at five-minute intervals. Measurements were corrected for barometric pressure using data collected from a PT placed in a nearby tree. Readings were converted to water depth above the transducer assuming hydrostatic conditions and a saline water density (1.025 g/cm^3) [*Fitts*, 2002]. PT3 was placed such that it was continuously submerged throughout the field campaign.

During both the 2017 and 2018 field campaigns, an anchor station was conducted at astronomical spring tide. The summer anchor station was 25 hours and the summer anchor station was 13 hours. Shipboard measurements of velocity profiles, suspended sediment, and near-bed velocity measurements were collected. The anchor stations were conducted within the tidal channel along Transect 12 (T12) (Fig. 2). Flow depth was continuously recorded using a Lowrance HDS-7 echo sounder, equipped with two dual frequency sonar heads, which provide downward single-beam sonar (50/200 kHz) as well as sidescan sonar (455/800 kHz). Velocity profiles were recorded during anchor stations using an acoustic Doppler current profiler (ADCP) recording at 2 Hz. The ADCP measurements were usable up to 0.25 m from the channel bottom due to reflection off the bed, so a mechanical velocimeter (Swoffer 3000) was deployed to measure near-bed velocity at 0.05, 0.15, 0.30, and 0.75 m above the bed at 30-minute intervals. Near-bed water samples were collected at 0.092 m above the channel bed every 30-minutes using an in situ pump system mounted on an instrumented tripod that could be lowered to and rest on the channel bed [*Sternberg et al.*, 1991]. These samples were analyzed for suspended sediment concentration (SSC) values. Water samples from the top ~0.2 m of the water column were obtained every hour with a bucket were used to determine suspended sediment concentration (SSC) using standard filtration, drying, and weighing techniques. Channel-bed sediment samples were collected at 30-minute intervals using a Petite Ponar Sampler and also subsequently analyzed for grain-size distribution using the Malvern Mastersizer 2000.

3.4 Mudflat Observations

Water depth and velocity were continuously monitored on the mudflat during the summer 2017 and winter 2018 field campaigns. Two PTs were deployed along T12 (i.e., PT1, PT2 Fig. 2) in an arrangement that covered the entire tidal elevation range on the mudflat when including PT3. The two PTs that were deployed on the mudflat were located at 178 m (PT2) and 331 m (PT1) from the channel bank (Fig. 2). The mudflat elevations are intertidal, and so PT1 and PT2 were not always submerged. PT measurements were collected every five minutes for 24 days in the summer, and 20 days in the winter. Readings were subsequently corrected for atmospheric pressure and converted to water depth assuming hydrostatic conditions and a saline water density (1.025 g/cm^3).

An Acoustic Doppler Velocimeter (ADV) was co-located with PT2 and provided point measurements of velocity 0.16 m above the mudflat. The ADV measured at 16 Hz at 30-second burst intervals, however data are only available when the ADV is inundated with water (i.e., >

0.36 m above the mudflat bed). Data collected by the ADV is subject to the quality control standards outlined in *Elgar [2005]*.

3.5 Analytical Framework for Suspended Sediment in the Tidal Channel

At rising tide, sediment-laden water emerges from the tidal channel and inundates the adjacent mudflat. Sediment deposition occurs as particles settle from the water, as is expected with slowing flow velocity onto the flat, and especially with slack tide conditions [*Friedrichs*, 2011]. This style of sediment movement to the mudflat is analyzed using a model that predicts mass exchange between the tidal channel and the mudflat. Here the parameters of this model are described.

The vertical SSC profile for the tidal channel, discretized for a grain size *i*, is given by:

$$\frac{c_i}{c_{b_i}} = \left[\frac{(H-Z)/Z}{(H-b)/b}\right]^{P_{R_i}}, \qquad \text{Eq. 1}$$

where c_i is the concentration of the i^{th} grain size evaluated at an elevation Z above the bed, where H is the total flow depth, and P_{Ri} is the Rouse number:

$$P_{Ri} = \frac{w_{si}}{\kappa u_*}, \qquad \text{Eq. 2}$$

w_{si} is the settling velocity of the i^{th} grain size, where settling velocities for particles that exceed 40 µm are determined by *Dietrich [1982]* and particles less than 40 µm are assumed to be flocculated and are assigned a w_s of 1 mm/s [*Warner et al.*, 2008; *Smith and Friedrichs*, 2011]. κ = 0.4 is the dimensionless von Kármán constant, u_* is the shear velocity, and b is the top of the bedload layer [*Wiberg and Rubin, 1989]*:

$$\frac{b}{D_{50}} = \frac{A_1 T^*}{1 + A_2 T^*}, \qquad \text{Eq. 3}$$

where A_1=0.68 and A_2 is a function of the median grain diameter of bed sediment, D_{50}:

$$A_2 = 0.0204(lnD_{50})^2 + 0.022(lnD_{50}) + 0.0709,$$

and T^* is the dimensionless ratio:

$$T_i^* = \frac{\tau_b}{\tau_{ci}}, \qquad \text{Eq. 4}$$

where $\tau_b = \rho u_*^2$ is the boundary shear stress, ρ = 1.025 g/cm^3 is the water density and τ_c is the critical shear stress of grain mobility for grain size i , which is set a set value of 0.04 for all grain sizes. A single value for τ_c is used because the bed sediment possesses a particle size range that produces cohesion (clay and silt), and therefore a single-particle entrainment function may not be appropriate. Recent studies have shown that multi-particle aggregate entrainment is common for silt [*Van Maren et al.*, 2009].

The sediment concentration at the top of the bedload layer is computed using the *McLean [1992]* entrainment relationship:

$$c_{bi} = F_i \frac{0.004(1-\varphi)E_i}{1+0.004E_i}, \qquad \text{Eq. 5}$$

where F_i is the fraction of grain size i of the total distribution, φ = 0.35 is the sediment bed porosity and $E = T^*\text{-}1$ is the transport stage. The individual grain size class distributions are summed to produce a complete concentration profile.

Model inputs constrained through field observation include: 1) grain-size distribution of bed material, 2) flow depth (H), and 3) shear velocity (u_*, determined by fitting a law-of-the-wall logarithmic velocity profile to mechanical velocimeter data; e.g., *Garcia, [2008],*). Bed material entrainment is calculated for 35 discreet logarithmically-spaced grain-size classes ranging 1 – 350 μm for three u_* values (20th, 50th, and 80th percentile of measured u_*). Volumetric SSC and grain-size distribution are calculated at 0.04 m intervals. The model is evaluated for each bed sample collected in order to characterize a range of possible SSC profiles. The finest bed sample distribution will generate maximum SSC, and the coarsest bed sample distribution will generate the lowest predicted SSC.

4 Results

4.1 Elevation and Bathymetry

The elevation and bathymetry data reveal that the tidal channel in AC1 deepens and widens as it approaches the Bohai Sea (Fig. 2-a), reaching a depth of ~5 m near the shoreline of the abandoned deltaic lobe. No expression of tidal channel levees are discernable from the elevation data. The seaward-dipping slope of the tidal channel bed is 2×10^{-4} and the mudflat dips seaward with a slope of 9.8×10^{-5}. The old levees of the Qingshuigou lobe are up to 1.5 m above the mudflat surface, with the highest relief located landward and a steady decrease toward the Bohai Sea (Fig. 2).

4.2 Sedimentological Data

Of the 17 extracted cores, nine display an abrupt contact between a thick (~5 m) silty-sand package and an overlying mud deposit ~0.3–1.8 m thick (Fig. 3). Eight cores display mud and sand interbedded, and maintain an overall fining-upward trend. For cores that penetrated to 6 m, the bottom typically displays interbedded mud and sand (Fig. 3). For all cores, silty-sand packages are massive (meters thick), with intervals of shallow-dipping foresets; however, no fine stratigraphy is observed, as the operation of the vibracore likely perturbed small structures.

Of the 45 pits that were excavated, a mud-sand contact was resolvable in 25, with an average depth of the mud-sand contact located at 0.19 m below the mud flat surface. In six pits, where the mud-sand contact was not reached before encountering the water table, this contact is assumed > 0.40 m below the surface. For pits near the tidal channel, there is often no obvious mud-sand transition. Instead, a mud layer caps centimeter-scale mud and sand laminae (14 pits). Generally, far from the tidal channels (> 60 m), it is possible to identify an abrupt mud-sand contact. Mud thickness, grain size (50^{th} and 90^{th} percentiles), and sorting were examined as a function of distance from the primary tidal channel (Fig. 4-a) and with distance from the shoreline (Fig. 4-b). No spatial trends in thickness, grain size, or sorting are discernable.

Grain-size distributions from massive sand deposits in the cores were compared to bed sediment samples collected from the active Huanghe channel [*Ma et al.*, 2017]. A two-sample Kolmogorov–Smirnov (K-S) test (Fig. 5-a) shows that the grain-size distributions are from the same continuous distribution with a 5% significance level. A two-sample K-S test was also used to compare randomly chosen core samples to randomly chosen active channel bed samples (Fig.

5-b). For 69% of the tests, the two samples are from the same continuous distribution, while 31% reject that the samples are from the same continuous distribution, at a 5% significance level.

4.3 Tidal Channel Observations

4.3.1 Summer 2017

The highest tidal range recorded by the PT in the tidal channel was 1.6 m (Fig. 6-a), coinciding with spring tide. Tides are mixed near spring tide (i.e., larger range between lower high and higher high tide, Fig. 6-a). At neap tide, the tidal range is 1 m, and the tides are less mixed (i.e. smaller range between lower high and higher high tide, Fig. 6-a). The TCM-1 located at T12 recorded near-bottom velocity up to 1 m/s, occurring during an ebb flow of spring tide (Fig. 6-b).

Anchor station measurements were collected over a 25-hour period during a spring tide. The median grain sizes for the seven samples collected from the tidal channel bed during the anchor station is 42–78 µm (Fig. 6-d). Water depth in the channel is 0.9–2.5 m (Fig. 7-a). Depth averaged velocity recorded by the ADCP is up to 1.1 m/s (Fig. 7-b), with the fastest velocity recorded during ebb flow. Near-bottom velocity collected using the mechanical velocimeter ranges up to 0.9 m/s. These data are used to estimate shear velocity, u_*, assuming a law-of-the-wall relationship (Fig. 7-c). Near-bottom volumetric SSC measurements are 2×10^{-5}–2×10^{-3} (Fig. 7-d) and the surface sediment concentration measures 1.5×10^{-5}–5.8×10^{-4} (Fig. 7-e). Not surprisingly, the highest concentration measured for both the near-bottom and the surface samples correspond to the highest recorded velocity and shear stress.

4.3.2 Winter 2018

PT data collected within the tidal channel document a tidal range of 0.6–2.7 m. The lowest range is associated with a neap tide, while the highest range is associated with an EAWM wind event compounded with a spring tide (Fig. 6-e). The TCM velocity data show that the highest velocity in the channel occurs during storm events and higher high spring tide, with the maximum velocity recorded during ebb flow (1 m/s). The lowest velocity occurs during fair weather and neap conditions at slack tide (Fig. 6-f). Water depth in the tidal channel is strongly correlated to high wind velocity directed from the northeast (Fig. 8). At the onset of winter storms, wind velocity is 35-40 kph, and water elevation achieves a maximum value during the observation period (i.e., ~2 m). With the cessation of high wind, water depth decreases, yet the spring/neap signatures remain obscured (Fig. 8).

A 13-hour anchor station was conducted one day after a large northeasterly wind event. At the onset of the wind event, the mudflat was inundated with 1.20 m of water. However, throughout the 25-hour anchor station, no inundation occurred on the mudflat. Furthermore, water depth was too low to collect resolvable ADCP data. The mechanical velocimeter measured near-bed velocity up to 0.3 m/s. During the storm event, the TCM located at T12 was fully inundated and recorded velocity up to 1 m/s. However, during the anchor station, the TCM was not submerged due to low water level, rendering the data unusable. Overall, SSC during the winter anchor station was relatively low compared to the summer anchor station measurements. Near-bottom SSC measured during the anchor station was $2.3 \times 10^{-5} – 4.7 \times 10^{-4}$. Surface SSC measurements range $2.4 \times 10^{-5} – 4.2 \times 10^{-4}$. At all sample intervals, the SSC measurements are similar at the channel bed and surface. The median grain size of the bed samples collected during the winter anchor station ranges 31–50 µm (Fig. 6-h)**.**

Measurements of water depth, velocity, and SSC during the winter anchor station do not reflect storm conditions. Most importantly, the conditions recorded do not provide any clear insight as to when sediment-laden water emerges onto the mudflat.

4.4 Mudflat Observations

During summer deployment, water inundated the mudflat during high tide for four days leading up to and following the spring tide (i.e., total of eight days of inundation). The maximum inundation was 0.5 m (Fig. 7-a). Following spring tide, the maximum daily water depth over the mudflat tapered until there was no inundation. The ADV located on the mudflat at T12, when sufficiently inundated, recorded velocity values that ranged from 0.01–0.20 m/s at 0.16 m above the mudflat (Fig. 9-a). The records indicate that the highest velocity occurs with the onset of flood tide, and the waning of the ebb tide. During slack tide, velocity was as low as 0.01 m/s and lasted 480-1400 s.

EAWM events observed during the winter survey amplified high tide so as to produce enhanced water depth on the mudflat (Fig. 9-b). PT measurements recorded up to 1.20 m of water inundating the mudflat during northeasterly wind events. However, with the cessation of high velocity northeasterly winds, tides were suppressed so that high tide did not inundate the mudflat until > 24 hours after the wind events ceased. Throughout the monitoring period, the ADV located on the mudflat at T12 recorded velocity values that ranged from 0.10–0.60 m/s at 0.16 m above the mudflat (Fig. 9-b).

4.5 Suspended Sediment Concentration Model

The anchor station conducted during summer 2017 provides a dataset to constrain suspended-sediment profiles for conditions when water inundates the mudflat (Eqns. 1–4, Fig. 10). Using a shear stress value determined from near-bottom velocity profiles (Fig. 7-c), Equation 1 predicts that over the range of measured flow conditions and sediment composition, the top 0.5 m of the water column maintains a volumetric SSC of $2{,}5 \times 10^{-7}$–2×10^{-3}. Comparing predicted and measured values, SSC profiles encompass the range of measured SSC. For SSC measurements, a washload concentration value ($2\text{x}10^{-5}$) has been removed from the total concentration, as determined by SSC concentrations at the top of the water column during slack tide. These lower 20th percentile of SSC measurements overlap the model for SSC using the 20th percentile u_*, and the upper 80th percentile SSC measurements overlap the model for SSC using the 80th percentile u_*. SSC Measurements between the 20th and 80th percentiles overlap the SSC model generated with the 50th percentile u_* value (Fig. 10).

The model is applied for the 20th, 50th, and 80th percentile measured u_* values and concomitant water depths. An important assumption is that sediment suspended to elevations higher than the adjacent mudflat surface is transported onto the mudflat. Using the measured range of slack tide duration (480–1400 s, and defined as velocity < 5 cm/s [Renshun, 1992]), sediment settles at each particle's settling velocity. The resulting grain-size distribution of the deposit is compared to measurements. It is determined that the grain-size distribution of particles settling during a slack tide duration of 400–600 seconds predicts the best match compared to measurements (Fig. 11). In this scenario, the finest sediment (<40 μm) is treated as flocculated and maintains a w_s of 1 mm/s [*Smith and Friedrichs*, 2011].

The observed and modeled relationship between u_* and SSC using different τ_c is shown in Figure 12. At low u_* values, all predicted near-bed SSC are within the range of measured field values (grey asterisks), however, for all τ_c, departure between model and measurement occurs with increasing u_*. SSC profiles in Figure 10 are generated using the lowest τ_c value in Figure 12, because higher τ_c values fail to entrain sediment at τ_b values determined during the anchor station. However, it should be noted that the SSC model does not match the shape of the observed SSC measurements at any tested value of τ_c. Furthermore, this value of τ_c is an order of magnitude lower than values reported in modeling papers for cohesion in deltaic environments [*Edmonds and Slingerland*, 2009; *Lanzoni and D'Alpaos*, 2015], as well as field observations of the entrainment of consolidated cohesive material [*Dunne et al.*, 2019]. In environments with fine sediment, τ_c is sensitive to the time duration over which consolidation can occur. For this system, where tides are mixed and semidiurnal, slack tide is typically less than 600 s and so there is little time for consolidation. This could be why relatively low values of τ_c provide best model fits to observed SSC measurements (Fig. 10).

5.0 Discussion

The extent of infilling of abandoned distributary channels, and the tendency for them to remain as topographic lows on a fluvial deltaic landscape, could influence the potential to reoccupy abandoned channels as flow pathways upon future avulsions. Evaluating the processes that impact the morphology of abandoned channels and their associated lobes is therefore important to understand overall delta evolution. In this study, sedimentation patterns of the abandoned Qingshuigou deltaic distributary channel and its lobe are evaluated. This particular lobe is unique because its channel was completely cut off from an upstream input of sediment and water, so its evolution is dictated by marine and atmospheric processes. During low tide, water is contained in the tidal channel and the mudflat is exposed; conversely, at high tide, sediment-laden water inundates the mudflat (Fig. 13-a, b, c, d). Meanwhile, seasonal wave and wind patterns affect water elevation and sediment concentration along the channel and across the mudflat. Filling of the channel must be accomplished with marine-derived sediment due to its cutoff from the primary Huanghe. The magnitude and timing of sedimentation processes are assessed using measurements of sediment and hydrodynamic properties. These data are used to validate a model for timing and magnitude of channel filling, which over time converts the abandoned channel into a mudflat.

5.1 Sedimentation and Stratigraphy Patterns of the Qingshuigou Channel Fill

The shallow stratigraphy of the abandoned Qingshuigou channel demonstrates a grain-size transition that is interpreted to reflect a change from sediment accumulating as part of the active river channel (fluvial origin) to mudflat sedimentation (marine origin). This assertion is bolstered by two-sample K-S tests that show that sediment grain-size distributions of the sand from the lower portions of channel cores and that of the bed material found in the modern Huanghe are indistinguishable (Fig. 5). This implies that the sand is channel bed material deposited by the active river before abandonment. Meanwhile, due to the cutoff from the active fluvial channel, the mud deposited in the channel (i.e., overlying the sand) must be derived from a marine source.

The overlying mud that drapes the antecedent fluvial deposit ranges in thickness from approximately 0.1 to 1.78 m (Fig. 4-a,b). The grain-size distribution of samples show no spatial (vertical, horizontal) trends (Fig. 4-a,b). These observations are atypical of what is found for many tidal flats: as fluid velocity and shear stress diminish away from the tidal channel, sediment deposit thickness and grain size typically reflect this gradient and systematically thin and fine, respectively [*Friedrichs*, 2011; *Flemming*, 2012]. Indeed, there seems to be no relation in terms of marine-derived sediment thickness and distance from the primary tidal channel (Fig. 4-b). Instead, we speculate that the fluvial channel topography was left to be inundated by water and sediment upon abandonment; in essence, the fluvial channel features were "frozen" in place upon avulsion, and subsequently buried by marine sediment. To first order, it is expected that the distribution of mud thickness varies inversely to the elevation of the former channel topography. To test this supposition, Landsat imagery of the channel prior to abandonment were used to delineate the location of the channel thalweg and bars (Fig. 14a).

Figures 14-b,c show the interpreted thalweg and bars, and core locations coded based on mud thickness (respectively). While it is not possible to know the exact elevations within the antecedent channel, the thalweg is inferred based on the location of water during a low discharge condition, while the bar tops are assessed based on the presence of the lighter buff color, interpreted to indicate relatively dry sediment (compared to the darker sediment adjacent to the water, which is interpreted to be saturated). Comparing locations within the antecedent thalweg and on the bar tops (Fig. 14-d), mud thickness over channel bars is on the scale of decimeters, and no greater than 0.65 m (Fig. 14-d), with a mean thickness of 0.18 m. For the core locations identified to have been collected in the former thalweg, mud deposit thickness is much higher and approaches 1.8 m, and averages 0.26 m.

This analysis indicates that the mud deposit is thicker over the antecedent thalweg, and thins overtop former bars. This supports the hypothesis that spatial variability in mud thickness is conditioned by the underlying antecedent channel topography left behind after an avulsion, rather than variable accumulation rates based on proximity to the tidal channel. Still, the notion that marine-derived mud passively infills the channel features of the abandoned Qingshuigou channel is bolstered by understanding water and sediment exchange between the tidal channel and the adjacent mudflat. These assessments constrain sedimentation rates and therefore the timing of channel filling and conversion to a mudflat.

5.2 Field Measurements to Constrain Sedimentation in the Qingshuigou Channel

Tidal inundation of the Qingshuigou lobe channel varies seasonally. In fair weather (summer) months, flooding patterns are dominated by spring/neap and semidiurnal cycles, with ~0.5 m of water covering the mudflat during higher high spring tide (Fig. 6-a,b). During winter months, spring/neap cycles are disrupted by high storm surge water levels associated with episodic EAWM (Fig. 6-e,f). At the onset of a wind event, tidal fluctuations are enhanced by strong wind from the northeast, and high-high spring tide inundates the flat with ~1.2 m of water. However, following the initial high-water event, northeasterly wind speed decreases, which dampens tidal amplitude (Fig. 12).

To evaluate the seasonal changes in water and sediment inundating the Qingshuigou mudflat, we calculate a width averaged water flux (q_w) (Eq. 6) using ADV (u, m/s) and PT data (h, m/s):

$$q_w = u * h. \qquad \text{Eq. 7}$$

When the ADV is not fully submerged (i.e., water over the mudflat is <0.36 m), q_w is estimated using a linear regression function fit to the calculated values (Fig. 15). The time-integrated water flux to the mudflat over a summer spring/neap cycle is 0.27 m^2/s, and for winter this value increases to 0.38 m^2/s.

Sediment flux to the mudflat is estimated as the product of q_w and sediment concentration of the surface water samples collected during the anchor station when the adjacent mudflat was inundated. Hence, it is assumed that the near-surface SSC measurements from the channel represent SSC of water moving onto the adjacent mudflat [*Mariotti and Fagherazzi*, 2012]. To calculate location and magnitude of sediment deposition, it is assumed that the suspended material settles through the water and deposits at a lateral distance from the tidal channel characterized by an advection length, L_a [*Ganti et al.*, 2014a]:

$$L_a = u\frac{h}{w_s}, \qquad \text{Eq. 8}$$

where h = 0.16 m (the location above the mudflat where the ADV measures flow velocity), u is the measured flow velocity, and w_s is the settling velocity of the 50th percentile grain size of the sample population. All particles are presumed to deposit on the mudflat. The inundation intermittency is determined based on PT measurements that include several spring/neap cycles.

The volume of water transferred from the tidal channel to the mudflat during the summer (integrated over the time of the anchor station, 25 hours, which captures one diurnal tidal cycle) is 186.2 m^2. The sediment transferred to the mudflat (S_a), based on measured concentration values, is 0.03 m^2 (Fig. 15-b). L_a is calculated for the 10th, 50th, and 90th percentile of the time averaged measured flow velocities recorded during inundation (i.e., 0.03 m/s, 0.07 m/s, and 0.09 m/s, respectively). A total vertical aggradation, V_a, is calculated over the tidal cycle by:

$$V_a = \frac{S_a}{L_a}. \qquad \text{Eq. 9}$$

Using the range of L_a values estimated, the resulting V_a outcomes over a diurnal tidal cycle are 2.0–6.7 × 10^{-3} m. Assuming a porosity of 30% [*Morris and Johnson*, 1967], a 70% annual inundation intermittency (based on field observation of the number of days the flat is inundated over a spring/neap cycle), and the range of L_a values (i.e., 10th, 50th, and 90th percentile), the annual V_a values are 0.68, 0.95, and 2.22 cm, respectively. These values are inherently conservative because the calculation does not include winter observations for the basic reason that *in-situ* measurements of SSC for surface water were not obtained when the mudflat was inundated, due to safety considerations. Nevertheless, other measurements of SSC collected during the winter field campaign show higher SSC than summer. Furthermore, there is greater inundation depth and longer inundation time over the mudflat during the winter relative to the summer conditions, particularly during storms; both conditions should produce enhanced mudflat sedimentation.

In cores and pits, measured values of mud deposition range from decimeters to meters for over the past twenty years (since abandonment), suggesting centimeter-scale annual rate of mud accumulation if the sedimentation rate is constant. Based on the previous analysis indicating thinner mud deposits over former fluvial bars and thicker mud deposits within the former thalweg (Fig. 14), it is inferred that overall accumulation *rates* for the past twenty years vary spatially as a consequence of the underlying fluvial topography. This makes sense, considering that low points are preferentially inundated with sediment-laden water, and the elevation of bar tops, which possess very little mud cover, are intermittently inundated (i.e., only during spring high-high tide). For example, considering the range of mud thickness values measured in the cores, assuming that this represents the totality of mud deposited since abandonment twenty years ago, the average accumulation rate near the abandoned channel thalweg is 1.3-8.9 cm/yr, and the average accumulation rate for locations outside the thalweg is ~0.8 cm/yr (Fig. 14). This latter value, and the lower range of the former value, are consistent with the annual rates of sedimentation estimated in the advection-settling analyses presented above. These estimates are caveated in several ways, including: seasonal variability in sediment delivery to the mudflat as a consequence of greater water inundation, and possibly greater sediment concentration, as measured during the energetic winter months, and the assumption that sediment delivered to the mudflat is deposited without bypass or subsequent removal.

Additionally, the grain size of sediment delivered to the mudflat may be predicted using a Rouse model [*Lanzoni and D'Alpaos*, 2015] informed by observations collected during the anchor station surveys within the adjacent tidal channel (Figure 11). The average grain-size distribution predicted by the Rouse model for the upper 0.5 m of the tidal channel water column (i.e., that portion of the flow assumed to inundate the mudflat) is determined, whereupon it is assumed that all of this material deposits to the mudflat (note: particles finer than 40 μm are assumed flocculated, and therefore possess a fixed settling velocity, as described above). This demonstrates that the calculated grain-size distribution of sediment transferred to the mudflat is remarkably similar to the sediment measured on the mudflat (Fig. 11).

Hence, both the rate of accumulation and grain size of sediment delivered from the tidal channel to the mudflat can be accounted for using basic models informed by observations collected from both the tidal channel and on the mudflat. Indeed, these assessments imply a sediment source derived locally, i.e. the tidal channel, as the Rouse model estimates the concentration of *bed material* sediment (as opposed to washload, which is inherently finer).

5.3 Constraining a Sediment Source for the Infilling of the Qingshuigou Lobe Channel

For non-deltaic fluvial channels abandoned by avulsion, channel infilling is facilitated by connectivity to the active channel and overbank sedimentation during floods. Abandoned deltaic distributary channels differ from their fluvial counterparts because the marine environment is an additional potential sediment source to fill the channel. For the Qinghsuigou channel, the analyses presented above indicate that suspended sediment transported by the tidal channel provides material that fills the former channel, converting the lobe into an aggrading mudflat. The active Huanghe channel plume, and/or the shallow subaqueous region of the Huanghe delta foreset, could both be possible sources of material to the tidal channel. However, as a point of comparison, the grain-size distributions of sediment collected from these environments compared to representative samples collected from the Qingshuigou mudflat (Fig. 16) show that both the sediment from the plume and delta foreset are much finer than that of the mudflat.

The grain-size distribution from the mudflat is most similar to the tidal channel bed, however there remains a seasonal contrast. For example, the median grain-size values of the channel bed are 42–78 μm for summer months (T12, Fig. 6-d), and 39–50 μm during winter months (Fig. 6-h). The fining of the tidal channel bed during the winter season could be associated with the enhanced wave climate of the adjacent Bohai Sea as a consequence of the EAWM [*Wang et al.*, 2014]. The EAWM resuspends fine sediment from the delta foreset, increasing sediment concentration in the adjacent marine environment [*Wang et al.*, 2014]. This sediment may move into the tidal channel, where it deposits. After the EAWM, wave energy is lower during quiescent summer months, and diurnal tidal currents rework the deposited sediment, suspending and transporting this material to the adjacent mudflat.

An additional factor to consider is that the Qingshuigou lobe is actively eroding and therefore its shoreline has receded since abandonment in 1996. In the twenty years since, the shoreline retreated 7 km, with an average retreat rate of ~431 m/yr between 1996 and 2013, and a retreat rate of ~184 m/yr between 2013 and present (Fig. 17). Wave energy, particularly during the winter months, is sufficient to remove and suspend sediment from the subaqueous portion of the lobe [*Wang et al.*, 2010]. This material is therefore readily transported via tidal currents into the abandoned Qingshuigou channel. Considering that the coastal system is eroding its own deltaic lobe sediment, this provides a source for the coarser material observed on the active mudflat, thereby accounting for the size fraction otherwise missing from the subaqueous foreset and active Huanghe plume.

5.4 Deltaic Channel Filling: To Completion, or Not?

For abandoned distributary channels, the ability to fill with sediment sourced from the marine basin is set by the tidal range, specifically, the higher-high spring tide elevation, assuming that this is the elevation to where sediment may be deposited via water-borne transport. In areas where the tidal range is large, it is shown that filling of an abandoned channel could be extensive [*Heath*, 2009]. An interesting case study comes from the Petitcodiac River in the Bay of Fundy (tidal range is ~7 m), where in 1968 a causeway was constructed, cutting off water and sediment to the lower 55 km of the river. This resulted in sedimentation in the abandoned channel downstream of the causeway (via tidal transport of marine sediment) and annealing the channel, which reduced its width by ~90% in twelve years (i.e., from 1 km to 100 m, [*Locke et al.*, 2003]). The thickness of the deposited sediment reached 8 m, consistent with the tidal range. For the abandoned Qingshuigou channel, micro-tidal conditions (~1.5 m) render tides incapable of reaching the elevation of the former channel levees, which presently extend up to 0.9 m above the higher high tide elevation (Fig. 2-c). Hence, it is expected that abandoned channels of the Huanghe cannot be completely filled (if the channels maintain a self-similar levee height).

Beginning in 1931, channel relocation of the Huanghe on its delta occurred through engineered avulsions (Fig. 1), most likely where a natural avulsion was pending [*Ganti et al.*, 2014]. Interestingly, for many of these artificial diversions (7 out of 8), the abandoned channel pathways are still discernable in satellite images, particularly in proximity to the node (i.e., cutoff point) of the avulsion. However, for all of these cases, sediment and water input to the abandoned channel were essentially instantaneously cutoff (as in the situation of the Qingshuigou channel). For natural avulsions (prior to 1931), it is not possible to identify abandoned channel bodies and, as demonstrated in Figure 1, these historical natural avulsions on the Huanghe delta tended to traverse new pathways, rather than reoccupy former channels [*Van Gelder et al.*, 1994]. It is therefore proposed that natural deltaic avulsions, with the capacity to maintain a connection to the primary channel, fill from both the upstream and downstream directions, as influenced by fluvial and marine processes, respectively. This, in turn, creates favorable conditions for complete sediment filling of the abandoned channel, and therefore limits the potential for reoccupation of former channels upon future avulsions. On the other hand, artificial avulsions are only capable of filling from the downstream direction and are thus limited in terms of filling by the upstream limit of tidal influence. Hence, it is expected that the remaining portion of these antecedent channels persist as topographic lows on the delta.

The lessons provided by the Huanghe delta indicate several important points. Under natural conditions, sediment delivery to an abandoned deltaic channel can arise from upstream (fluvial) and downstream (marine) sources. For the former, the tidal range, relative to the levee height, determines the degree to which the channel may fill. The elevation of fluvial channel levees is, to first order, dependent on river stage during floods [*Smith and Pérez-Arlucea*, 2008], which for deltaic channels is set primarily by water surface slope [*Nittrouer et al.*, 2012]. If the tidal range is low compared to the levee height (as in the case of the Qingshuigou lobe), then channels remain under-filled and topographic lows (Fig. 18-a). Alternatively, it is possible to fill abandoned channels if levee heights are comparable to the tidal range (Fig. 18-b). For the upstream (fluvial) situation, water and sediment input via connection to the main channel could work to fill the channel from upstream, which, when combined with downstream marine sediment, may work to fully anneal the abandoned channel. To elucidate patterns of marine sediment filling of abandoned distributary channels, it is necessary to constrain the possible range of tidal inundation relative to the elevation of the levee height when the channel was active. Furthermore, as documented herein, patterns of deposit grain size and thickness may not be predictable when there is exclusively marine sourced sediment. This is divergent from abandoned channels that maintain a connection to the active fluvial channel [*Gray et al.*, 2016]**.** In turn, these sedimentary signatures may prove useful for interpreting the rock record of ancient fluvial-deltaic systems.

6 Conclusions

Understanding the processes that lead to sediment infill of abandoned deltaic distributary channels has important implications for understanding delta dynamics, improving engineering practices, and interpreting the stratigraphic record. This study utilizes a modern example of the abandoned Qingshuigou distributary channel of the Huanghe, which was abandoned in 1996 via engineered avulsion, and has been subsequently filling with marine sediment delivered by tides. The shallow stratigraphy of the abandoned channel displays a transition from the formerly active channel to tidally delivered sediment. Observations of hydrodynamic conditions and sediment delivery within the abandoned channel confirm modern sediment accumulation.

On average, 0.50 m of mud has been deposited over the antecedent Qingshuigou fluvial channel bed. Stratigraphic observations, sediment flux monitoring, and modeling efforts indicate that modern accumulation rates on the mudflat are up to several centimeters per year. Field observations of mud thickness were explored for spatial trends, however no trends exist as a function of distance from the tidal channel bank or with distance from the shoreline. Instead, the antecedent topography of the Huanghe channel bed exerts a primary control on mud deposit thickness.

The sediment that comprises the tidal channel bed varies seasonally. Sediment that is suspended in the Bohai Sea during EAWM wave activity fines the tidal channel bed, where, throughout the remainder of the year, tidal currents rework and coarsen this material and transfer sediment onto the mudflat. The grain-size distribution of material present on the mudflat can be attributed to bed material of the tidal channel, and so sediment is assumed to be sourced locally.

The sedimentological record produced by infilling abandoned distributary channels provides insight for delta dynamics and the role of marine sediment delivery to nearshore environments. The degree of infilling, and spatial characteristics of sediment infill are indicative of marine vs. fluvial mechanisms for filling. The abandoned Qingshuigou levees exceed the elevation of the higher-high spring tide, so sediment sourced from the receiving basin is likely insufficient to fully anneal the channel.

Acknowledgments

This study was supported by the National Science Foundation (NSF) EAR-1427262, "Coastal SEES Collaborative Research: Morphologic, Socioeconomic, and Engineering Sustainability of Massively Anthropic Coastal Deltas: The Compelling Case of the Huanghe Delta." We would like to thank the Hydrological Survey Bureau of the Yellow River Mouth and the Yellow River Institute of Hydraulic Research for facilitating the logistics of this fieldwork. We also gratefully acknowledge field support from Tian Dong, Chenliang Wu, Eric Barefoot, Michelle Mullane, Katie Lavalle, Liang Chen, Michael Lamb, and Gary Parker. All data used for analyses and conclusions in this paper are provided within the document or within supplementary material.

References

Aalto, R., J. W. Lauer, and W. E. Dietrich (2008), Spatial and temporal dynamics of sediment accumulation and exchange along Strickland River floodplains (Papua New Guinea) over decadal- to- centennial timescales, *J. Geophys. Res. Earth Surf.*, *113*(F1), doi:10.1029/2006JF000627.

Aslan, A., and W. J. Autin (1999), Evolution of the Holocene Mississippi River floodplain, Ferriday, Louisiana; insights on the origin of fine-grained floodplains, *J. Sediment. Res.*, *69*(4).

Chamberlin, E. P., and E. A. Hajek (2015), Interpreting Paleo-Avulsion Dynamics from Multistory Sand Bodies, *J. Sediment. Res.*, *85*(2), 82–94, doi:10.2110/jsr.2015.09.

Chu, Z. X., X. G. Sun, S. K. Zhai, and K. H. Xu (2006), Changing pattern of accretion/erosion of the modern Yellow River (Huanghe) subaerial delta, China: Based on remote sensing images, *Mar. Geol.*, *227*(1–2), 13–30, doi:10.1016/j.margeo.2005.11.013.

Dunne, K. B. J., D. J. Jerolmack, E. Science, and A. Mechanics (2019), R ivers shaped by the most erosion resistant material, , 1–7.

Edmonds, D. A., and R. L. Slingerland (2009), Significant effect of sediment cohesion on delta morphology, *Nat. Geosci.*, 105–109, doi:10.1038/NGEO730.

Fitts, C. (2002), *Groundwater Science*, 1st ed.

Flemming, B. W. (2012), Siliciclastic Back-Barrier Tidal Flats, in *Principles of Tidal Sedimentology*, pp. 231–267, Springer Netherlands, Dordrecht.

Friedrichs, C. T. (2011), Tidal Flat Morphodynamics: A Synthesis, in *Treatise on Estuarine and Coastal Science*, vol. 3, pp. 137–170.

Ganti, V., M. P. Lamb, and B. McElroy (2014a), Quantitative bounds on morphodynamics and implications for reading the sedimentary record, *Nat. Commun.*, *5*(1), 3298, doi:10.1038/ncomms4298.

Ganti, V., Z. Chu, M. P. Lamb, J. A. Nittrouer, and G. Parker (2014b), Testing morphodynamic controls on the location and frequency of river avulsions on fans versus deltas: Huanghe (Yellow River), China, *Geophys. Res. Lett.*, *41*(22), 7882–7890, doi:10.1002/2014GL061918.

Van Gelder, A., J. H. Van Den Berg, G. Cheng, and C. Xue (1994), Overbank and channelfill deposits of the modern Yellow River delta, *Sediment. Geol.*, *90*, 293–305, doi:10.1016/0037-0738(94)90044-2.

Gray, A. B., G. B. Pasternack, E. B. Watson, and M. A. Goñi (2016), Abandoned channel fill sequences in the tidal estuary of a small mountainous, dry-summer river, *Sedimentology*, *63*(1), 176–206, doi:10.1111/sed.12223.

Hajek, E. A., and M. A. Wolinsky (2012), Simplified process modeling of river avulsion and alluvial architecture: Connecting models and field data, *Sediment. Geol.*, *257–260*, 1–30, doi:10.1016/J.SEDGEO.2011.09.005.

Heath, K. M. (2009), Fluid mud formation in the Petiticodiac River, New Brunswick, Canada, Boston College.

Le Hir, P., W. Roberts, O. Cazaillet, M. Christie, P. Bassoullet, and C. Bacher (2000), Characterization of intertidal flat hydrodynamics, *Cont. Shelf Res.*, *20*(12–13), 1433–1459, doi:10.1016/S0278-4343(00)00031-5.

Hoitink, A. J. F., P. Hoekstra, and D. S. van Maren (2003), Flow asymmetry associated with astronomical tides: Implications for the residual transport of sediment, *J. Geophys. Res.*, *108*(C10), 3315, doi:10.1029/2002JC001539.

Kim, W., D. Mohrig, R. Twilley, C. Paola, and G. Parker (2009), Is It Feasible to Build New Land in the Mississippi River Delta?, *Eos, Trans. Am. Geophys. Union*, *90*(42), 373–374, doi:10.1029/2009EO420001.

Lanzoni, S., and A. D'Alpaos (2015), On funneling of tidal channels, *J. Geophys. Res. Earth Surf.*, *120*(3), doi:10.1002/2014JF003203.

Locke, A., J. M. Hanson, G. J. Klassen, S. M. Richardson, and C. I. Aube (2003), The Damming of the Petitcodiac River: Species, Populations, and Habitats Lost, *Northeast. Nat.*, *10*(1), 39, doi:10.2307/3858671.

Ma, H., J. A. Nittrouer, K. Naito, X. Fu, Y. Zhang, A. J. Moodie, Y. Wang, B. Wu, and G. Parker (2017), The exceptional sediment load of fine-grained dispersal systems: Example of the Yellow River, China, *Sci. Adv.*, *3*(5), e1603114, doi:10.1126/sciadv.1603114.

Mackey, S. D., and J. S. Bridge (1995), Three-Dimensional Model of Alluvial Stratigraphy: Theory and Application, *J. Sediment. Res.*, *65*(1).

Van Maren, D. S., J. C. Winterwerp, Z. Y. Wang, and Q. Pu (2009), Suspended sediment dynamics and morphodynamics in the Yellow River, China, *Sedimentology*, *56*(3), 785–806, doi:10.1111/j.1365-3091.2008.00997.x.

Mariotti, G., and S. Fagherazzi (2012), Channels-tidal flat sediment exchange: The channel spillover mechanism, *J. Geophys. Res. Ocean.*, *117*(C3), n/a-n/a, doi:10.1029/2011JC007378.

Mohrig, D., P. L. Heller, C. Paola, and W. J. Lyons (2000), Interpreting avulsion process from ancient alluvial sequences: Guadalope-Matarranya system (northern Spain) and Wasatch Formation (western Colorado), *GSA Bull.*, *112*(3), 1787–1803.

Morris, D. A., and A. I. Johnson (1967), Summary of hydrologic and physical properties of rock and soil materials, as analyzed by the hydrologic laboratory of the U.S. Geological Survey, 1948-60, *Water Supply Pap.*

Nienhuis, J. H., A. D. Ashton, P. C. Roos, S. J. M. H. Hulscher, and L. Giosan (2013), Wave reworking of abandoned deltas, *Geophys. Res. Lett*, *40*, 5899–5903, doi:10.1002/2013GL058231.

Nittrouer, J. A., J. Shaw, M. P. Lamb, and D. Mohrig (2012), Spatial and temporal trends for water-flow velocity and bed-material sediment transport in the lower Mississippi River, *Geol. Soc. Am. Bull.*, *124*(3–4), 400–414, doi:10.1130/B30497.1.

Pang, J., and S. Si (1979), The Estuary Changes of the Huanghe River I. Changes in Modern Time, *Oceanol. Limnol. Sin.*, *10*(2), 136–141.

Reitz, M. D., D. J. Jerolmack, and J. B. Swenson (2010), Flooding and flow path selection on alluvial fans and deltas, *Geophys. Res. Lett.*, *37*(6), doi:10.1029/2009GL041985.

Ridderinkhof, H., R. van der Ham, and W. van der Lee (2000), Temporal variations in concentration and transport of suspended sediments in a channel–flat system in the Ems-Dollard estuary, *Cont. Shelf Res.*, *20*(12), 1479–1493, doi:10.1016/S0278-4343(00)00033-9.

Roberts, H. (1997), Dynamic changes of the Holocene Mississippi River Delta Cycle, *J. Coast. Res.*, *13*(3), 605–627.

Rowland, J. C., K. Lepper, W. E. Dietrich, C. J. Wilson, and R. Sheldon (2005), Tie channel sedimentation rates, oxbow formation age and channel migration rate from optically stimulated luminescence (OSL) analysis of floodplain deposits, *Earth Surf. Process. Landforms*, *30*(9), 1161–1179, doi:10.1002/esp.1268.

Saito, Y., H. Wei, Y. Zhou, A. Nishimura, Y. Sato, and S. Yokota (2000), Delta progradation and chenier formation in the Huanghe (Yellow River) delta, China, *J. Asian Earth Sci.*, *18*(4), 489–497, doi:10.1016/S1367-9120(99)00080-2.

Slingerland, R., and N. D. Smith (2004), River Avulsions and Their Deposits, *Annu. Rev. Earth Planet. Sci*, *32*, 257–285, doi:10.1146/annurev.earth.32.101802.120201.

Smith, N. D., and M. Pérez-Arlucea (2008), Natural levee deposition during the 2005 flood of the Saskatchewan River, *Geomorphology*, *101*(4), 583–594, doi:10.1016/J.GEOMORPH.2008.02.009.

Smith, N. D., T. A. Cross, J. P. Dufficy, and S. R. Clough (1989), Anatomy of an avulsion, *Sedimentology*, *36*(1), 1–23, doi:10.1111/j.1365-3091.1989.tb00817.x.

Smith, S. J., and C. T. Friedrichs (2011), Size and settling velocities of cohesive flocs and suspended sediment aggregates in a trailing suction hopper dredge plume, *Cont. Shelf Res.*, *31*, S50–S63, doi:10.1016/j.csr.2010.04.002.

Sternberg, R. W., G. C. Kineke, and R. Johnson (1991), An instrument system for profiling suspended sediment, fluid, and flow conditions in shallow marine environments, *Cont. Shelf Res.*, *11*(2), 109–122, doi:10.1016/0278-4343(91)90057-D.

Toonen, W. H. J., M. G. Kleinhans, and K. M. Cohen (2012), Sedimentary architecture of abandoned channel fills, *Earth Surf. Process. Landforms*, *37*(4), 459–472, doi:10.1002/esp.3189.

Wang, A., N. Bi, X. Zeng, and H. Xiao (2014a), Seasonal distribution of suspended sediment in the Bohai Sea, China, *Cont. Shelf Res.*, *90*, 17–32, doi:10.1016/j.csr.2014.03.006.

Wang, H., N. Bi, Y. Wang, Y. Saito, and Z. Yang (2010), Tide-modulated hyperpycnal flows off the Huanghe (Yellow River) mouth, China, *Earth Surf. Process. Landforms*, *35*(11), 1315–1329, doi:10.1002/esp.2032.

Wang, H., A. Wang, N. Bi, X. Zeng, and H. Xiao (2014b), Seasonal distribution of suspended sediment in the Bohai Sea, China, *Cont. Shelf Res.*, *90*, 17–32, doi:10.1016/j.csr.2014.03.006.

Wang, Z.-Y., and Z.-Y. Liang (2000), Dynamic characteristics of the Yellow River mouth, *Earth Surf. Process. Landforms*, *25*(7), 765–782, doi:10.1002/1096-9837(200007)25:7<765::AID-ESP98>3.0.CO;2-K.

Warner, J. C., C. R. Sherwood, R. P. Signell, C. K. Harris, and H. G. Arango (2008), Development of a three-dimensional, regional, coupled wave, current, and sediment-transport model, *Comput. Geosci.*, *34*(10), 1284–1306, doi:10.1016/J.CAGEO.2008.02.012.

Wright, L. D., and C. A. Nittrouer (1995), Dispersal of River Sediments in Coastal Seas: Six Contrasting Cases, *Estuaries*, *18*(3), 494, doi:10.2307/1352367.

Zhang, J., W. Wen Huang, and M. Chong Shi (1990), Huanghe (Yellow River) and its estuary: Sediment origin, transport and deposition, *J. Hydrol.*, *120*(1–4), 203–223, doi:10.1016/0022-1694(90)90150-V.

Zhang, P., Z. Li, and H. Wen (2012), Modernization of National Geodetic Datum in China, in *Nineteenth United Nations Regional Cartographic Confence for Asia and the Pacific ,* *United Nations Economic and Social Council*, pp. 1–6.

Zinger, J. A., B. L. Rhoads, and J. L. Best (2011), Extreme sediment pulses generated by bend cutoffs along a large meandering river, *Nat. Geosci.*, *4*(10), 675–678, doi:10.1038/ngeo1260.

Figure Captions

Figure 1. a) Map of eastern Asia, denoting the location of the Huanghe delta (within red square), which builds into the Bohai Sea. b) The Huanghe delta, which avulses every decade by abandoning an active channel in favor of a new pathway to the sea, which presently occurs through both natural processes and engineering practices. The active channel is represented by the blue line, and black lines locate prior channels (modified from: [*Pang and Si*, 1979; *Van Gelder et al.*, 1994; *Saito et al.*, 2000; *Chu et al.*, 2006]. c) Composite Sentinel-2 image assembled from images spanning November 2017-June 2018. Currently, some abandoned channel pathways are visible on the landscape, however, others are annealed (topographic lows that have subsequently filled with sediment). The Qingshuigou lobe was abandoned through engineering practices in 1996, and the node location is denoted by the black star. A tidal channel delivers water and sediment to the mudflats that occupy the abandoned Qingshuigou channel and lobe.

Figure 2. a) Elevation of the Qingshuigou channel and lobe, referenced to mean sea level. b) A photograph of the abandoned Qingshuigou channel, looking downstream, approximately 10 km from the Bohai Sea. Note the abandoned Huanghe levees, visible by occurrence of vegetation, which are ~ 600 m apart (i.e., width of the antecedent channel). A tidal channel and mudflat now occupy the abandoned channel. c) Transect 12 elevation cross-section (location shown in (a)), where monitoring instruments were deployed and where the 25-hr anchor station observations were collected to measure hydrodynamic and sediment conditions.

Figure 3. a) Map indicating the location for the 17 6-m long vibracores (white stars) and 45 pits excavated in the Qingshuigou lobe. b) Grain size of sediment collected in three cores, showing proportion of clay, silt and sand, referenced to depth below the surface. Note that mud dominates the shallower portion, while silt and sand fractions increase with depth.

Figure 4. a) Mud thickness, median grain size (D50), 90^{th} percentile coarsest sediment (D90), and sediment sorting for surface samples, plotted with respect to distance from the primary tidal channel (i.e., transverse to tidal channel axis). No spatial trends are evident from the data. b) Mud thickness, D50, D90, and sediment size sorting for surface samples, plotted with respect to

distance from the 2016 shoreline determined in a Landsat 8 image. Mud thickness is variable over this distance, and sorting, D50, and D90 are relatively consistent, with the data displaying no trend.

Figure 5. a) Grain-distributions from sand samples collected from cores, compared to samples collected from the active Huanghe channel bed, by using a two-sample Kolmogorov–Smirnov test. The result indicates that the average grain-size distributions of the sandy sediment from the cores is indistinguishable from active Huanghe (with a 5% significance level). b) A two-sample K-S test used to compare randomly chosen core samples to randomly chosen active Huanghe bed samples; for 69% of the tests, the two samples are from the same continuous distribution (with a 5% significance level).

Figure 6. Channel time series of water elevation, (a) and (e), near-bed velocity, (b) and (f), suspended-sediment concentration, (c) and (g), and grain size distributions of channel bed sediment with the solid line representing the mean of all samples, and the gray envelope bounded by dashed orange lines demarcates the maximum and minimum grain size sample distributions , with the average median grain size, D_{50}, noted. Note a-d (orange) represent summer measurements, and e-h (blue) represent winter measurements For both water depth and velocity in summer, the highest values are associated with spring tide. Suspended-sediment concentration for summer is only a three day period during spring tide. The largest values were measured at ebb tide (maximum concentration: ~700 mg/l. Overall average median value is 80 □m. Winter storms (March 4, 8, and 14) have an important impact. High values (>1 m/s) occur during winter storms. g) SSC, measured during a winter 2018. Values exceeded the limits of the OBS (1200 mg/l), whereupon the instrument recorded “0” values. Overall average median value is 60 □m.

Figure 7. Current speed and water depth data collected on the mudflat during the summer 2017 and winter 2018 field campaigns. Instruments were placed 150 m from the tidal channel bank, using a co-located ADV and pressure transducer (ADV and PT2, Fig. 2 a,c). Two weeks of water depth (solid blue line a-d) and speed (dashed red line, a-d) data were collected during summer (a) and winter (b). During summer (a), inundation patterns are dictated by astronomical spring-neap cycles, where the mudflat is inundated with up to 0.50 m of water during spring tide, while very

little inundation occurs during neap. During winter, storms associated with the EAWM perturb the astronomical tidal cycle, where the greatest inundation of the mudflat occurs during periods with high wind speed rather than the spring tide. The highest inundation on the mudflat corresponds to both spring tide and setup by strong northeasterly wind. Though the flats are inundated more frequently during the summer (a, b), the total water flux to the flats is 40 % greater in the winter (d) than during the summer (c) (3.83×10^3 vs. 2.73×10^3, respectively).

Figure 8. Summer 2017 survey anchor station data collected within the tidal channel at Transect 12 (Fig. 2-a, c), coinciding with spring tide, 24-25 June, 2017. a) Channel water depth below transducer, as recorded using a Lowrance single beam echosounder. b) Depth-averaged current speed measured by a ship-mounted ADCP. c) Shear velocity (u*), as calculated by using the law-of-the-wall estimate of velocity profiles. d) SSC measured from water samples collected 0.092 m above the tidal channel bed and e) SSC measured from water samples at the top ~0.2m of the water column.

Figure 9. Bed material concentration profiles modeled using the 20th, 50th, and 80th percentile u_* values (solid red, blue, and yellow lines, respectively) plotted to depth as normalized to the maximum spring tide water depth, for the summer 2017 anchor station at Transect 12 (Fig. 8-c). Solid lines are determined using the average grain-size distribution measured on the tidal channel bed; the gray envelopes depict the range of predicted SSCs for measured grain-size distributions. Measured near-bed and surface SSC are displayed by the gray asterisks. The measured SSC associated with the measured u_* value is displayed in like colors (i.e., red circles are measured SSC values for the 20th percentile u_*). For the 20th percentile u_* value, the measured SSC values fall within the envelope of predicted SSC. For the 50th and 80th percentile u_* values, the predicted SSCs overestimate the observed SSCs.

Figure 10. a) Near-bed volumetric SSC, measured using the near bottom water samples during the summer 2017 anchor station at Transect 12, plotted as a function of their corresponding estimated u_* (gray asterisk, shown in time-series in Fig. 8-c, d). The near-bed SSC predicted by Equation 4 is shown as the solid red line. At low u_* values (<0.015), the predicted SSC is within the range of the measured values, however there is significant data scatter. With increasing u_*,

Equation 4 over-predicts SSC values compared to the measured values. Coefficient α is evaluated by the best fit between measured and predicted SSC. The blue (50th percentile u_*) and yellow lines (80th percentile u_*) display the relationship between u_* and SSC when a coefficient (α) is applied. b) α is applied to each Rouse profile displayed in Figure 10, to produce SSC profiles that fit the range of measured values during the summer 2017 anchor station (Fig. 8-d, e). As u_* increases, a smaller α is necessary to produce a fit between model and data; conversely, a higher u_* means that the model over predicts measured SSC.

Figure 11. Gain size distributions of samples collected from the mudflat (locations shown in Fig. 3-a) as shown by the gray envelope, where the solid blue line denotes the average cumulative grain-size distribution. The dashed lines are cumulative grain-size distributions predicted to deposit for a time period of slack water (color coded accordingly), based on the sediment sizes for the top 0.5 m of the water column, calculated from a Rouse model for conditions measured during the summer 2017 field campaign. Note that the predicted grain-size distributions are closest to the measured values for longer slack tide duration. When slack tide is 600 s, flocculated material settles from the water column.

Figure 12. Wind velocity plotted with markers showing the direction the wind is going to (top plot), and wind speed and water depth (bottom plot), measured in the tidal channel on Transect 12 (Fig. 2-a, c) during the winter 2018 field survey. X-axis is date, as per month and day. At the onset of winter storms, high wind velocity corresponds to a large water depth in the tidal channel. With the cessation of high wind velocity, water depths decreased. Hourly wind data are sourced from World Weather Online.

Figure 13. Illustration (not to scale) representing sediment infill of the Qingshuigou abandoned channel. Sediment-laden water is conveyed by a tidal channel. During low tide (a,b), water is contained within the tidal channel. At high tide (c,d), sediment-laden water leaves the tidal channel and inundates the adjacent mudflat. SSC and grain size varies with elevation above the channel bed, Z (Figs.10, 11-a, Equation 1). Sediment is transported onto the mudflat and deposited, travelling a distance described by L_a (see Eqn. 7). Sediment deposits and drapes the

antecedent channel bed topography, creating a spatially variable thickness of fine sediment in the abandoned channel bed.

Figure 14. a) Landsat 5 image of the Qingshuigou lobe acquired May 31, 1996, one month prior to avulsion. b) Channel thalweg is identified based on the occurrence of water (blue line). The lighter buff color in this image is assumed to be dry sediment and therefore part of the relatively elevated channel bar tops (shown in pink). The thalweg and bars demonstrate variable channel topography**.** c) Core and pit data, with the thickness of the mud drape coded by color. d) Boxplots of mud thickness for cores and pits located on bar tops and within the thalweg. The mean mud thickness on the bar tops is 0.18 m while the mean thickness within the thalweg is 0.26 m. The total range of mud thickness on the bar tops is 0.65 m, while the range within the thalweg is up to 1.78 m.

Figure 15. a) Water flux as a function of depth of inundation, calculated based on velocity and depth data recorded on the mudflat by the ADV and pressure transducer, respectively. The relationship between depth (x-axis) and water flux (y-axis) is best fit by a linear regression, and this function is used to estimate water flux when the ADV head is not fully submerged. b) Water flux (blue line) as a function of time for a spring flood tide and ensuing inundation of the mudflat on June 24, 2017 at point PT2 (Fig. 2-c) on Transect 12. Sediment flux (red line) is estimated for the same location as the product of the spring flood tide water flux and the concentration measured at the top of the water column during the anchor station.

Figure 16. a) Grain size samples were collected from within the tidal channel (Transect 12, blue circle), mudflat (brown circles), active channel plume (yellow circle), subaqueous delta foreset (red circles), and disaggregated inorganic grain size of suspended sediment in tidal channel (collected at blue circle). b) The cumulative grain-size distributions of sediment collected at these location is shown for comparison. The tidal channel bed (including winter, summer, and spatially averaged samples) most closely resembles the mudflat distributions.

Figure 17. The Qingshuigou lobe distal shoreline position (1996–2018), extracted from satellite imagery, plotted as a distance from an inland datum. The shoreline retreated 431 m/yr from 1996-2012, and then slowed to 184 m/yr.

Figure 18. Illustration demonstrating abandoned channel fill potential in relation to the antecedent levee height. The channel bed and levee form when the channel is active. Upon abandonment, marine sediment transported by tides deposits in the channel and transforms the deposit into a mudflat. The degree to which the abandoned channel fills is a function of the tidal range (assuming water-borne transport of material) relative to the antecedent levee height. In (a), the levee height is higher than the tidal range, and so the abandoned channel cannot fully fill. In (b), the tidal range is large relative to the levee height and so it is possible to entirely fill the channel with sediment.

Figure.

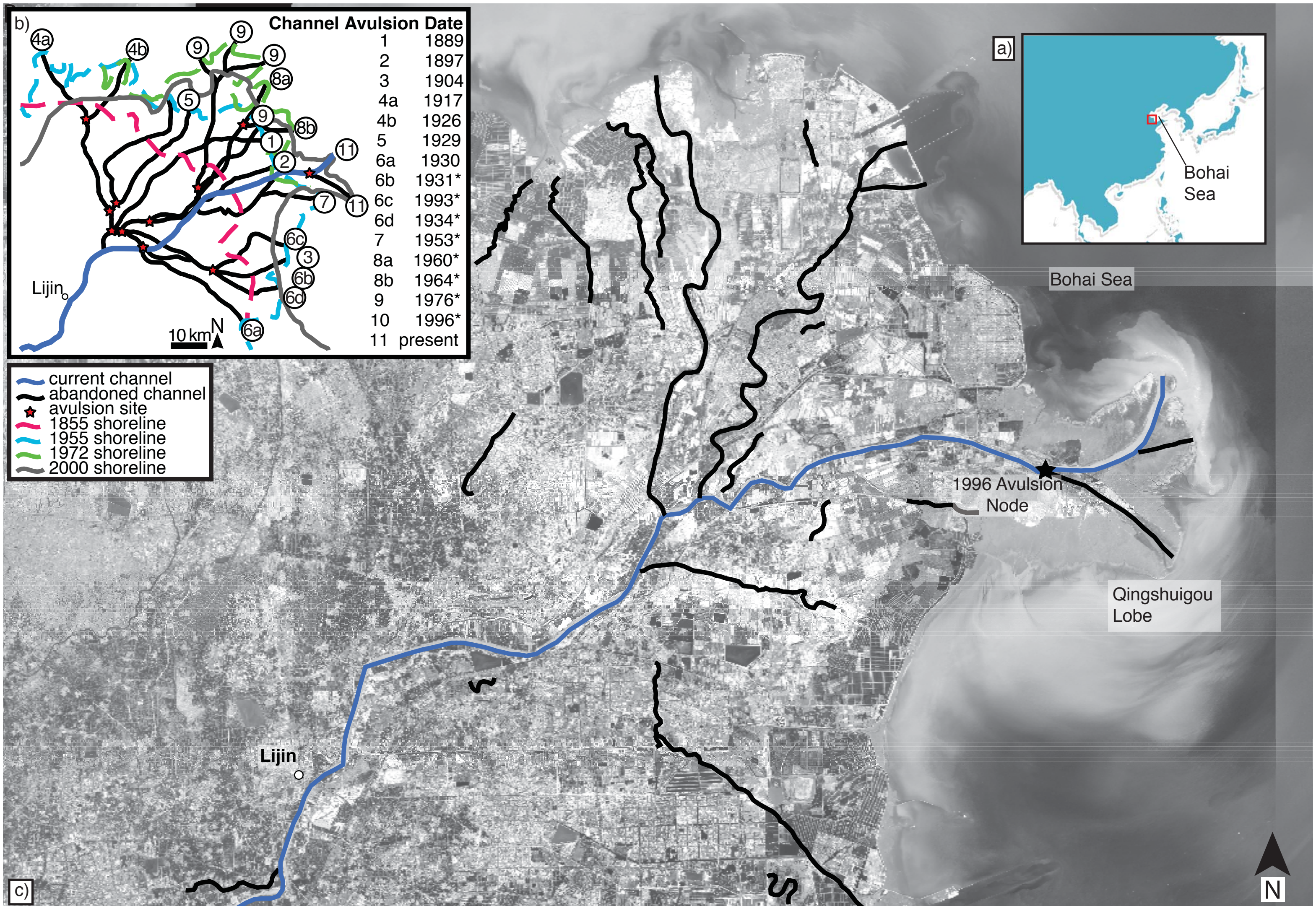

b)
Channel Avulsion Date
1 1889
2 1897
3 1904
4a 1917
4b 1926
5 1929
6a 1930
6b 1931*
6c 1993*
6d 1934*
7 1953*
8a 1960*
8b 1964*
9 1976*
10 1996*
11 present
Lijin
10 km
N
current channel
abandoned channel
avulsion site
1855 shoreline
1955 shoreline
1972 shoreline
2000 shoreline
a)
Bohai Sea
Bohai Sea
1996 Avulsion Node
Qingshuigou Lobe
Lijin
c)
N

Figure 1

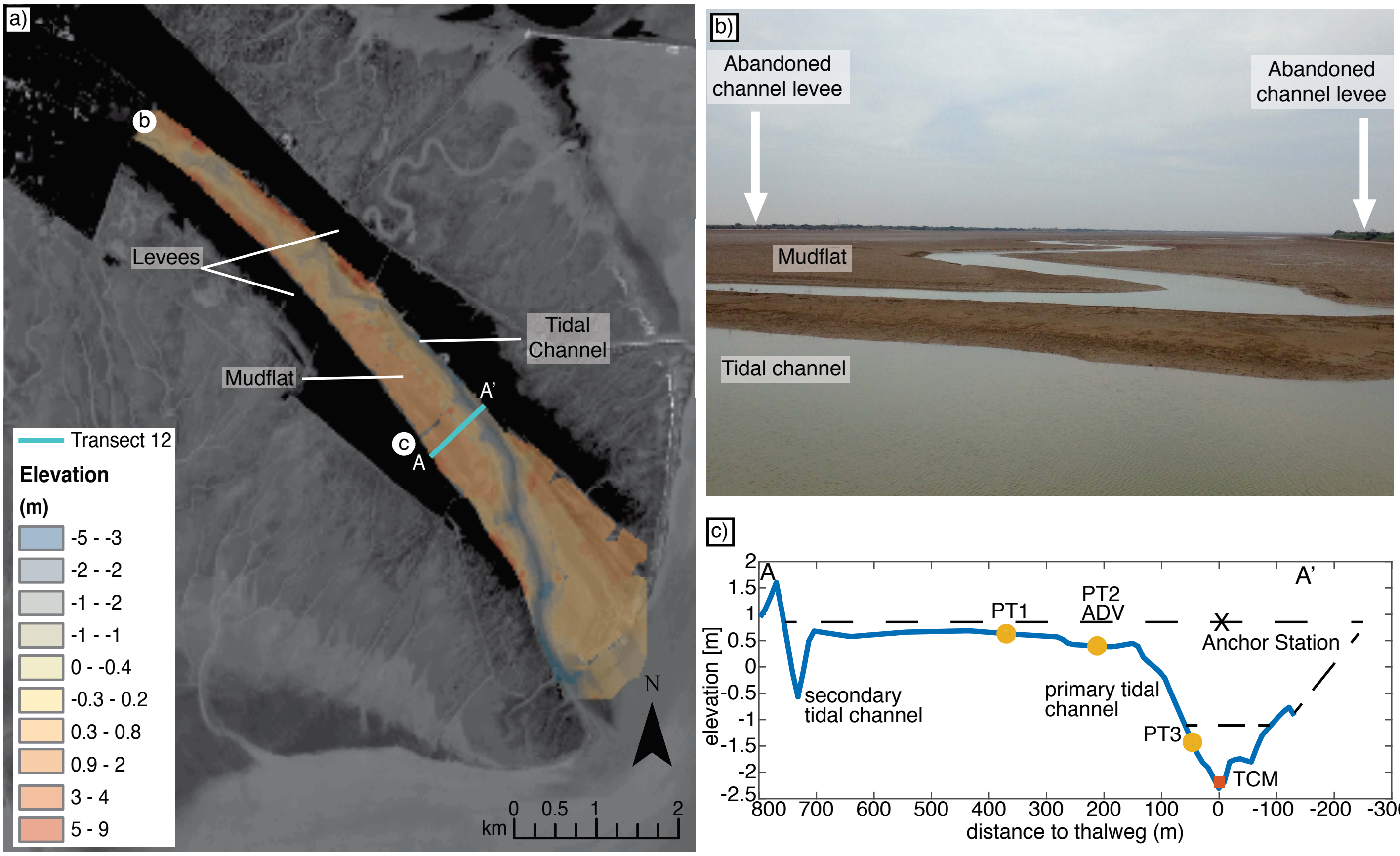
a)
b
Levees
Tidal Channel
Mudflat
A'
c
A
Transect 12
Elevation (m)
-5 - -3
-2 - -2
-1 - -2
-1 - -1
0 - -0.4
-0.3 - 0.2
0.3 - 0.8
0.9 - 2
3 - 4
5 - 9
N
0 0.5 1 2
km
b)
Abandoned channel levee
Abandoned channel levee
Mudflat
Tidal channel
c)
A
A'
PT1
PT2
ADV
Anchor Station
secondary tidal channel
primary tidal channel
PT3
TCM
elevation [m]
distance to thalweg (m)

Figure 2

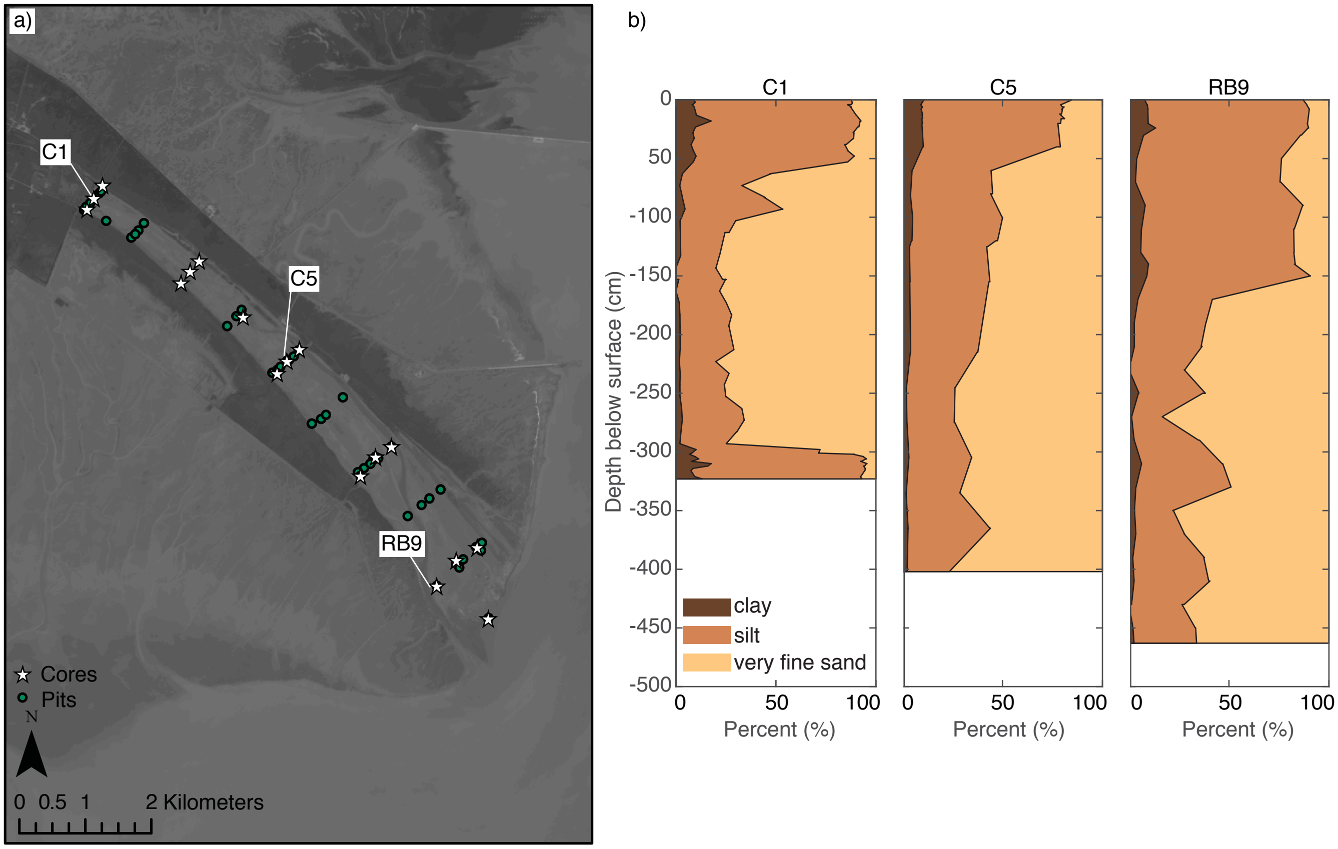
a)
C1
C5
RB9
Cores
Pits
N
0 0.5 1 2 Kilometers
b)
C1
C5
RB9
Depth below surface (cm)
0
50
-100
-150
-200
-250
-300
-350
-400
-450
-500
clay
silt
very fine sand
0 50 100
Percent (%)

Figure 3

4

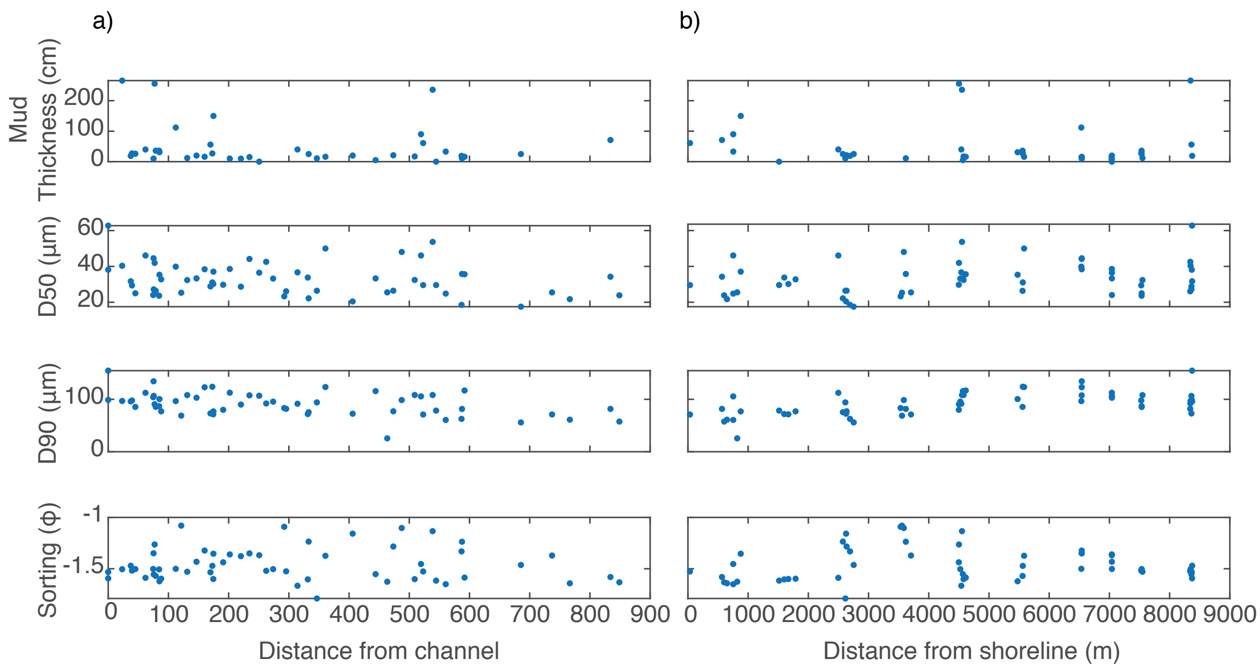
a)
b)
Mud Thickness (cm)
200
100
0
D50 (µm)
60
40
20
D90 (µm)
100
0
Sorting (ϕ)
-1
-1.5
0
100
200
300
400
500
600
700
800
900
Distance from channel
0
1000
2000
3000
4000
5000
6000
7000
8000
9000
Distance from shoreline (m)

5

a.

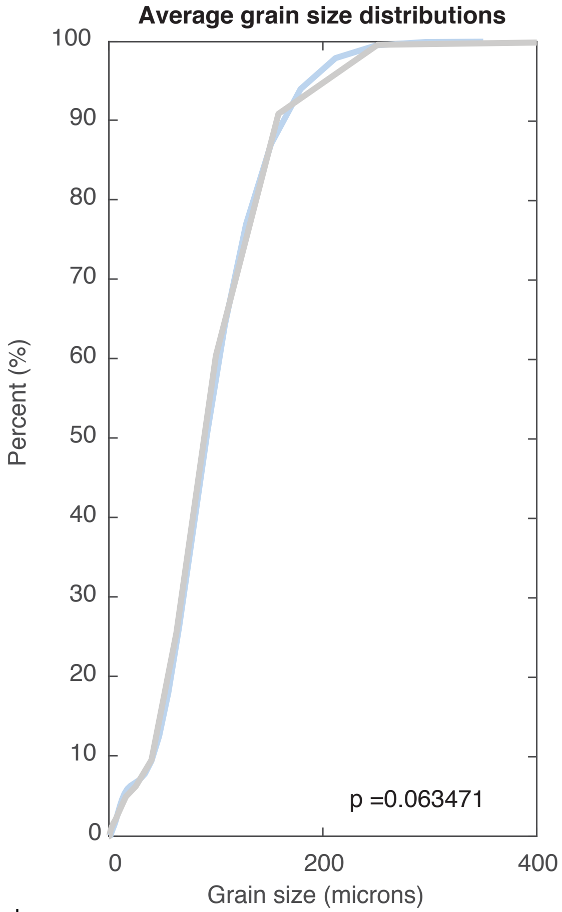

Average grain size distributions
100
90
80
70
60
50
40
30
20
10
0
Percent (%)
p =0.063471
0
200
400
Grain size (microns)

b.

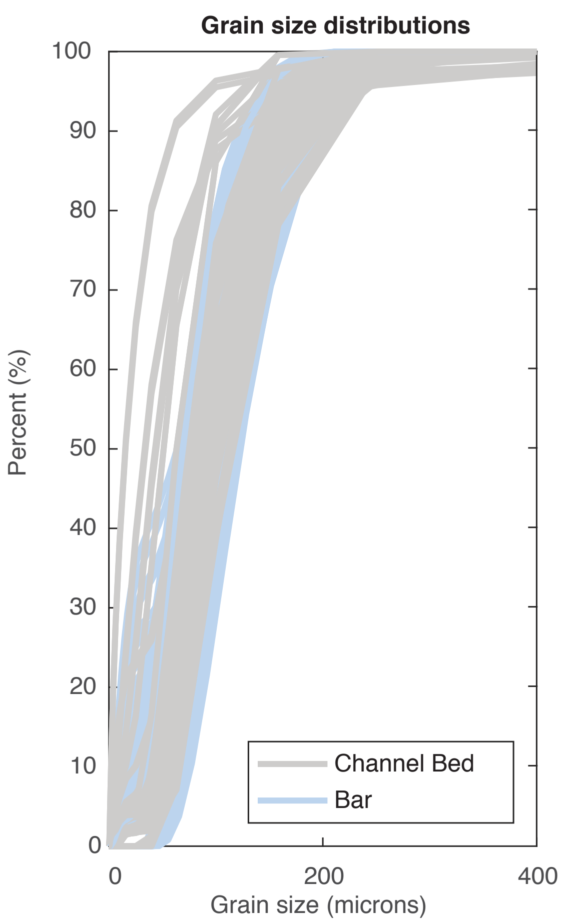

Grain size distributions
100
90
80
70
60
50
40
30
20
10
0
Percent (%)
Channel Bed
Bar
0
200
400
Grain size (microns)

Figure 6

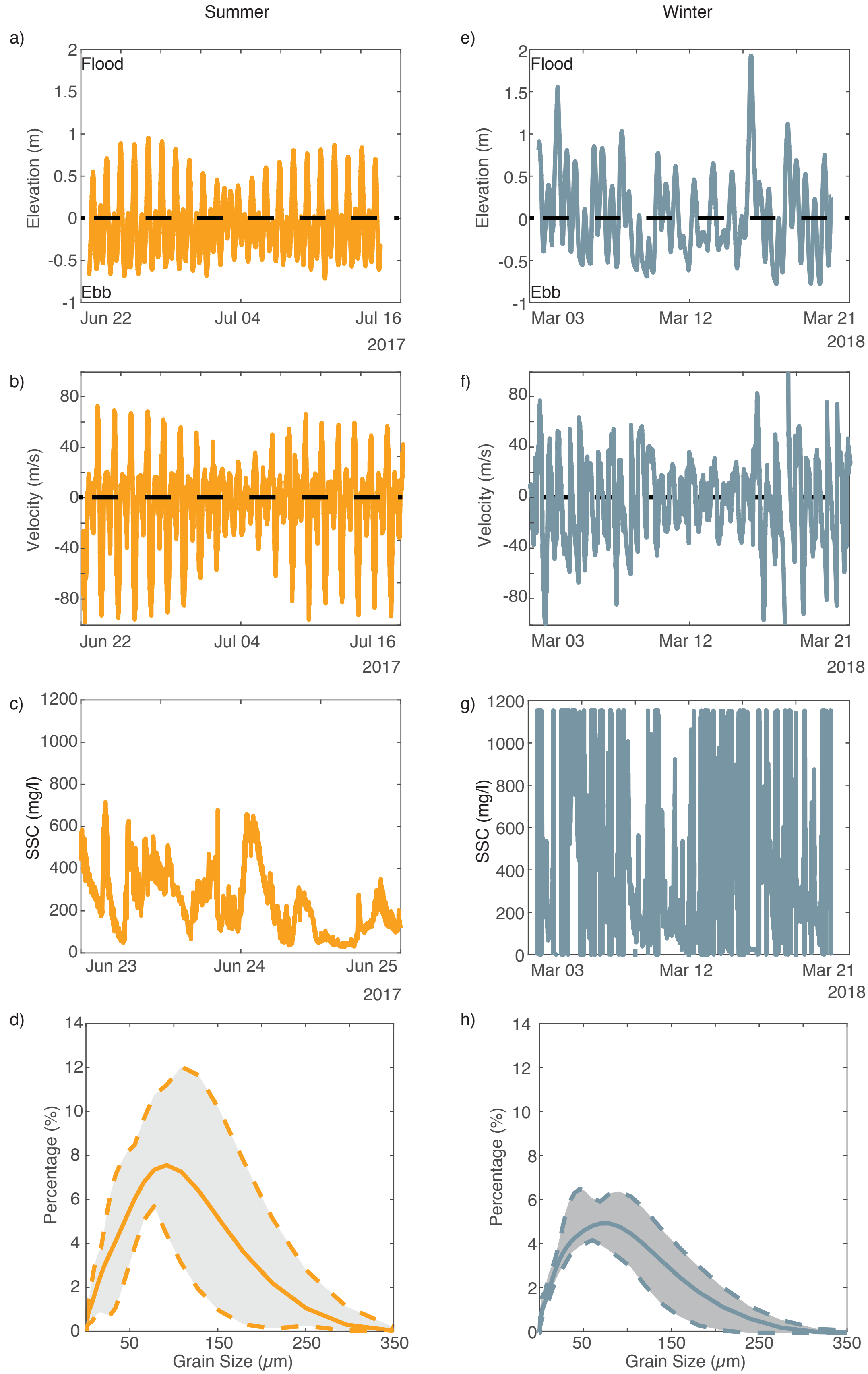

Summary
Winter
a)
Flood
Ebb
Elevation (m)
Jun 22
Jul 04
Jul 16
2017
e)
Mar 03
Mar 12
Mar 21
2018
b)
Velocity (m/s)
f)
c)
SSC (mg/l)
Jun 23
Jun 24
Jun 25
g)
d)
Percentage (%)
Grain Size (μm)
h)

Figure 7

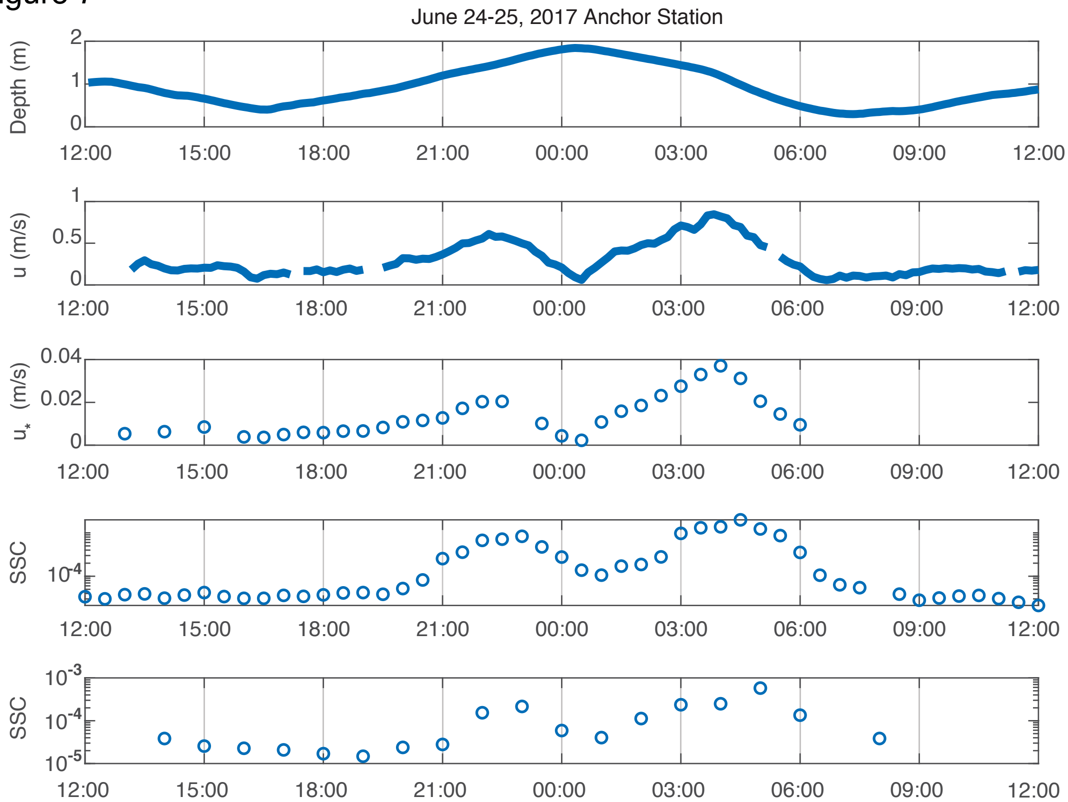

June 24-25, 2017 Anchor Station
a.
Depth (m)
b.
u (m/s)
c.
u_* (m/s)
d.
SSC
e.
SSC
12:00
15:00
18:00
21:00
00:00
03:00
06:00
09:00
12:00

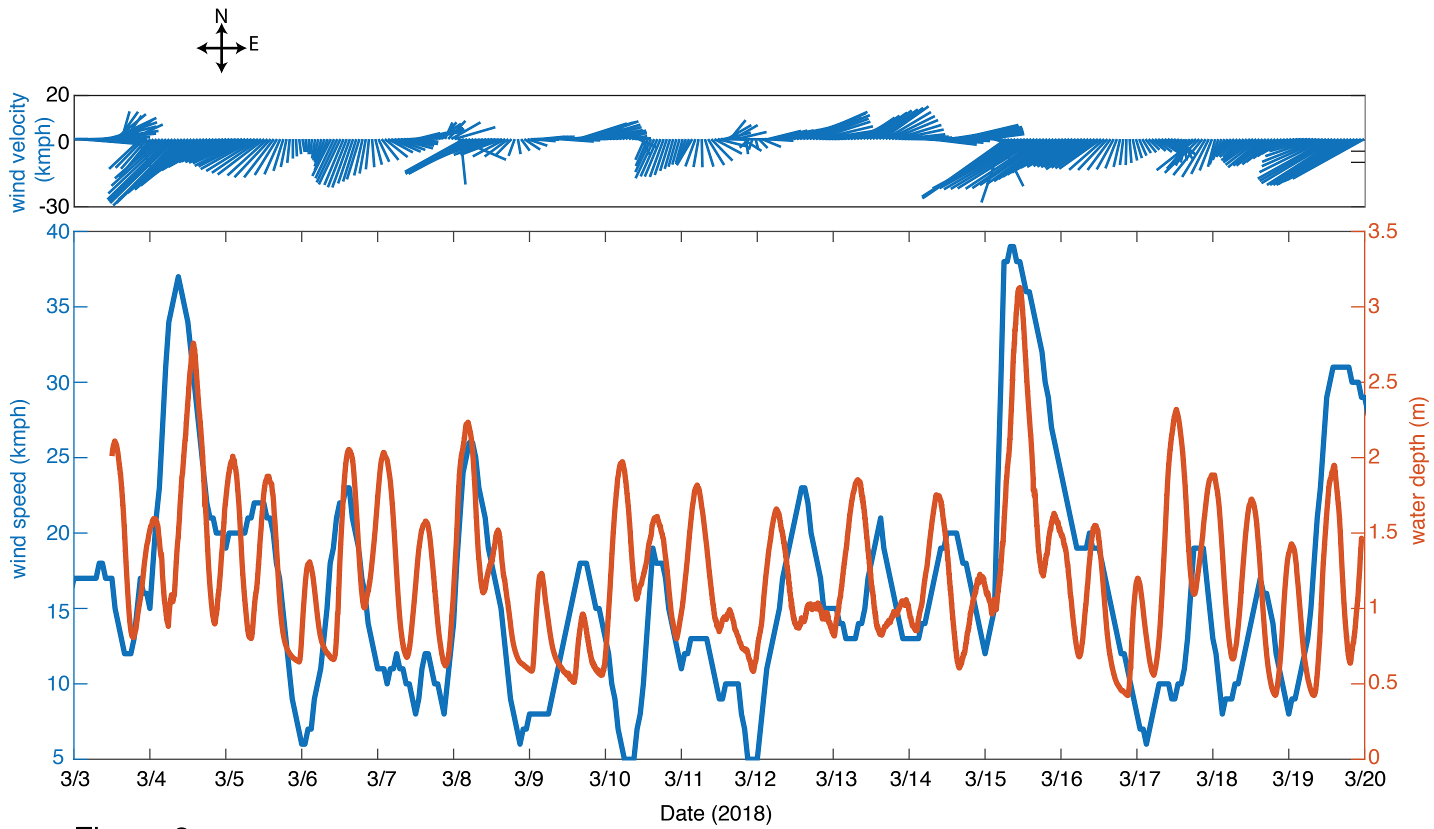

N
E
wind velocity (kmph)
20
0
-30
40
35
30
25
20
15
10
5
wind speed (kmph)
3.5
3
2.5
2
1.5
1
0.5
0
water depth (m)
3/3
3/4
3/5
3/6
3/7
3/8
3/9
3/10
3/11
3/12
3/13
3/14
3/15
3/16
3/17
3/18
3/19
3/20
Date (2018)

Figure 8

Figure 9

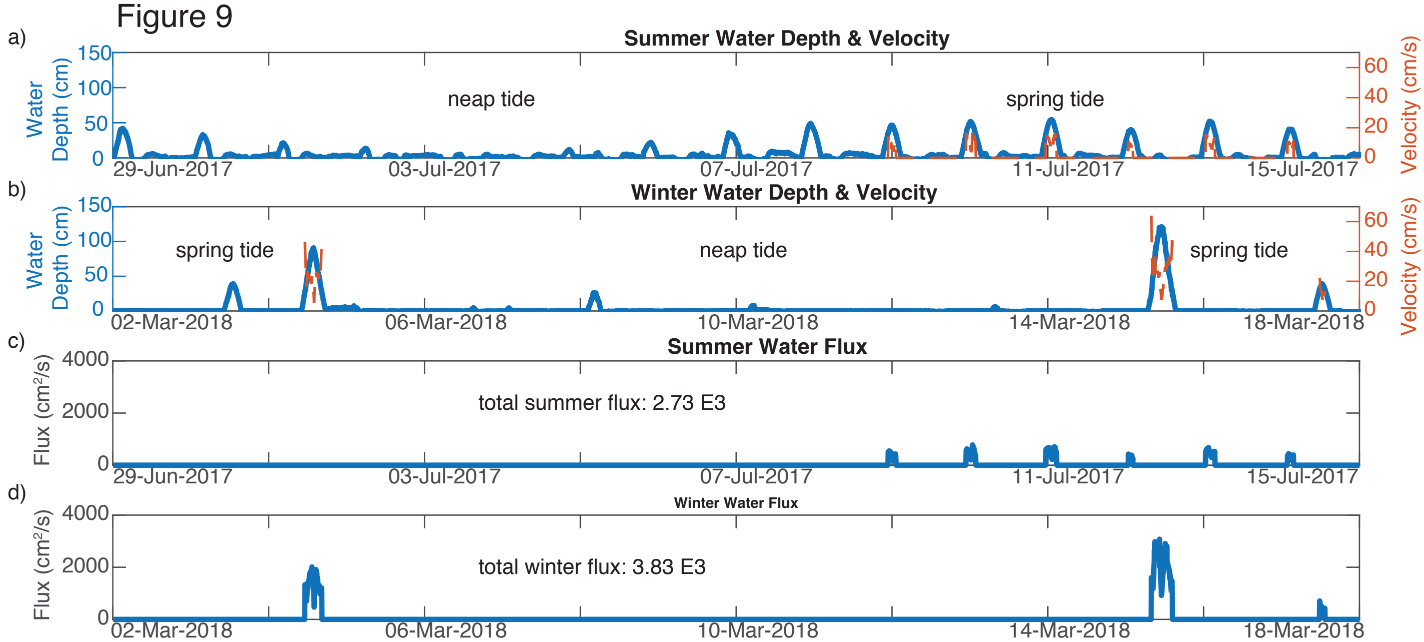

a)
Summer Water Depth & Velocity
Water Depth (cm)
Velocity (cm/s)
neap tide
spring tide
29-Jun-2017
03-Jul-2017
07-Jul-2017
11-Jul-2017
15-Jul-2017
b)
Winter Water Depth & Velocity
spring tide
neap tide
spring tide
02-Mar-2018
06-Mar-2018
10-Mar-2018
14-Mar-2018
18-Mar-2018
c)
Summer Water Flux
Flux (cm²/s)
total summer flux: 2.73 E3
d)
Winter Water Flux
total winter flux: 3.83 E3

Figure 10

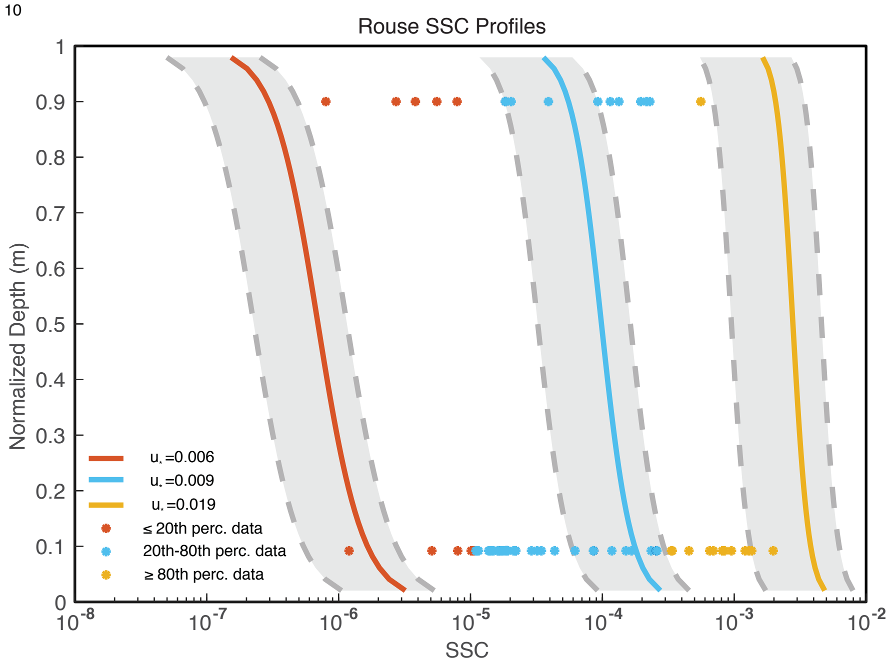
Rouse SSC Profiles
Normalized Depth (m)
SSC
u* =0.006
u* =0.009
u* =0.019
≤ 20th perc. data
20th-80th perc. data
≥ 80th perc. data
0
0.1
0.2
0.3
0.4
0.5
0.6
0.7
0.8
0.9
1
10-8
10-7
10-6
10-5
10-4
10-3
10-2

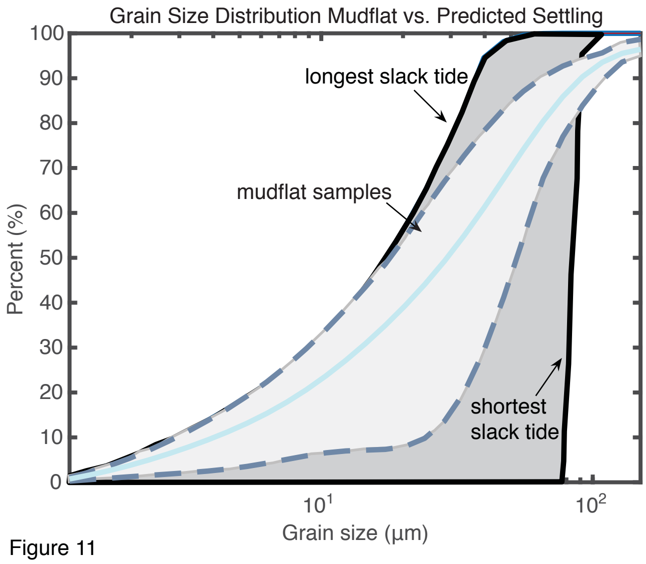
Grain Size Distribution Mudflat vs. Predicted Settling
100
90
80
70
60
50
40
30
20
10
0
Percent (%)
longest slack tide
mudflat samples
shortest
slack tide
10^1
10^2
Grain size (μm)

Figure 11

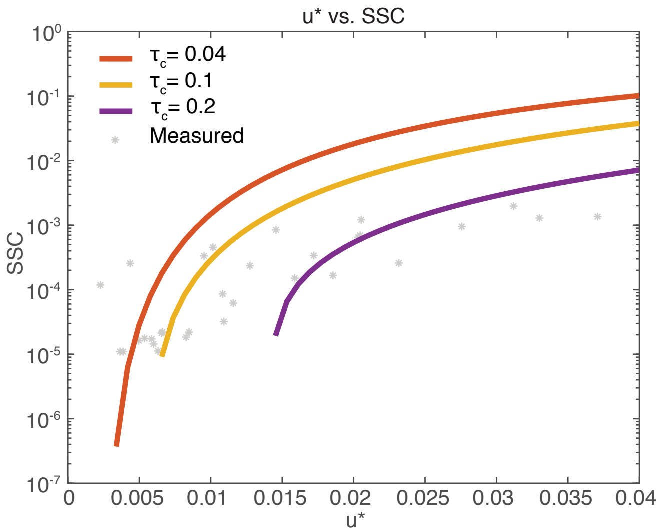
u* vs. SSC
τ_c= 0.04
τ_c= 0.1
τ_c= 0.2
Measured
SSC
10^{0}
10^{-1}
10^{-2}
10^{-3}
10^{-4}
10^{-5}
10^{-6}
10^{-7}
0
0.005
0.01
0.015
0.02
0.025
0.03
0.035
0.04
u*

Figure 12

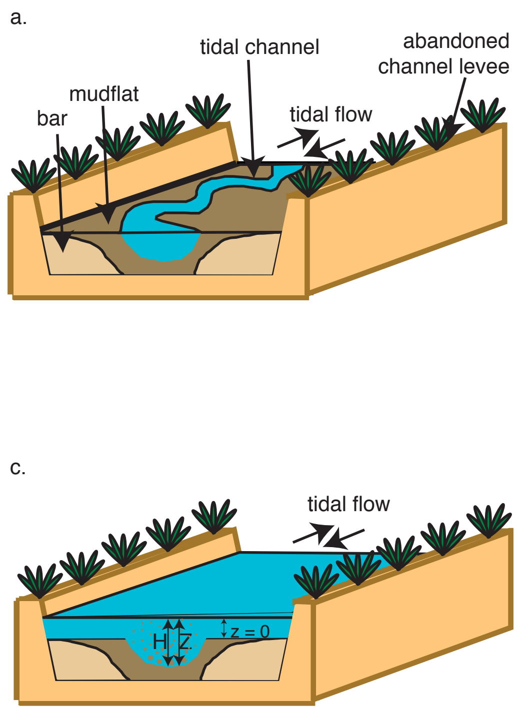
a.
tidal channel
abandoned
channel levee
mudflat
tidal flow
bar
b.
H
c.
tidal flow
H
Z
z = 0
d.
tidal flow
La
H
Z

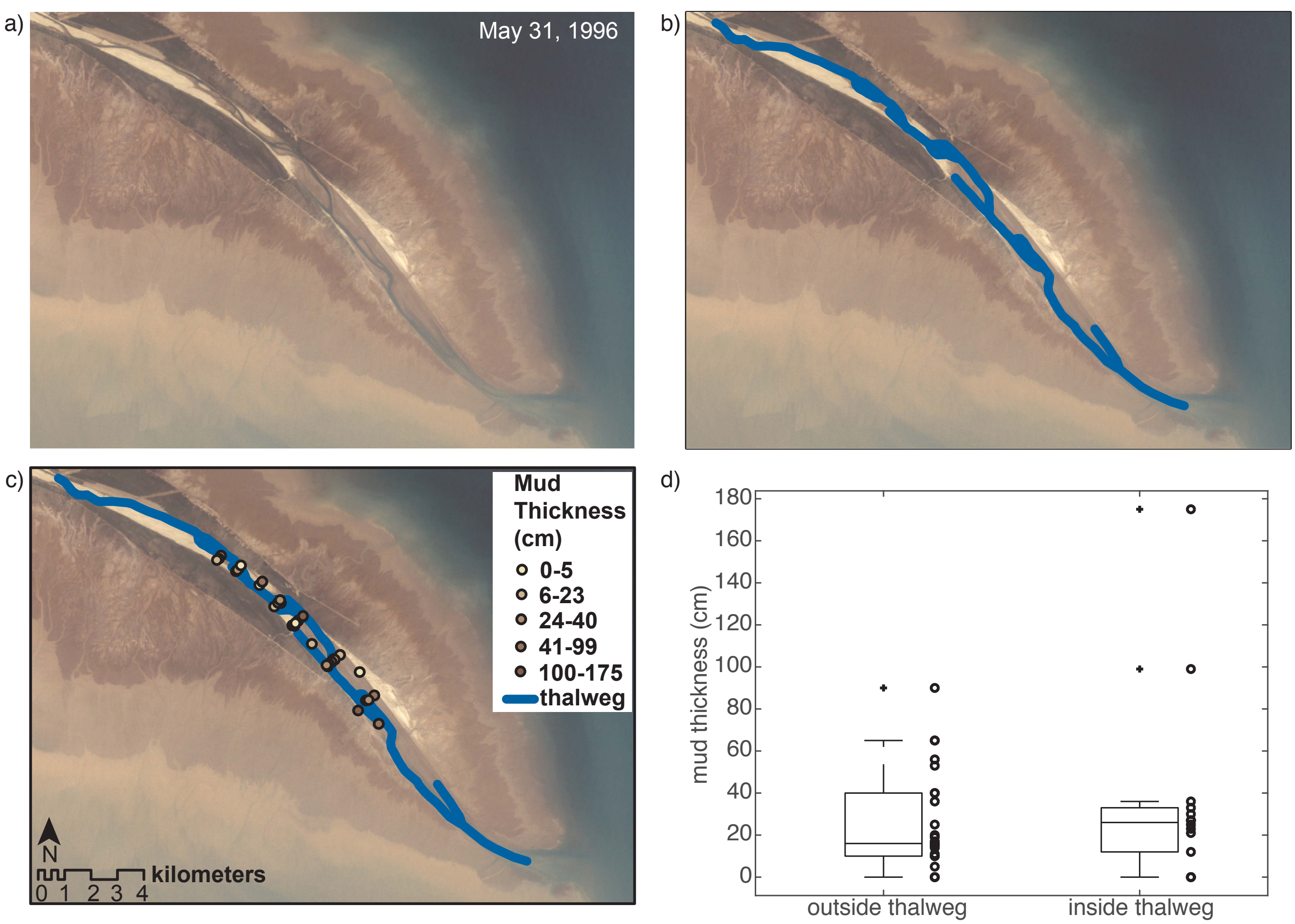
a)
May 31, 1996
b)
c)
Mud Thickness (cm)
0-5
6-23
24-40
41-99
100-175
thalweg
N
0 1 2 3 4 kilometers
d)
mud thickness (cm)
180
160
140
120
100
80
60
40
20
0
outside thalweg
inside thalweg

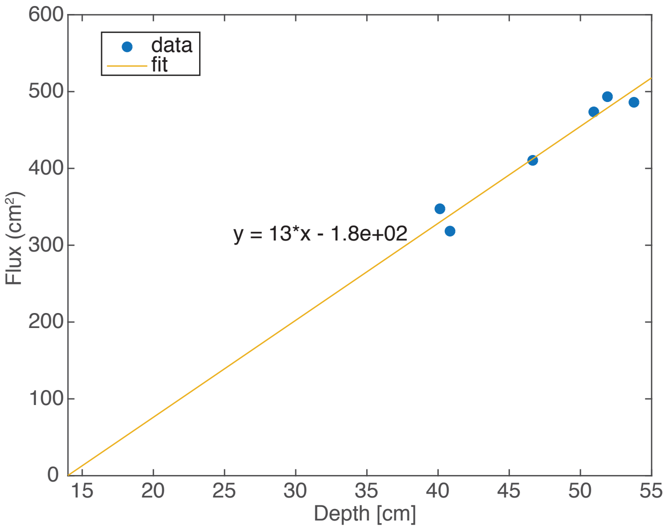
data
fit
y = 13*x - 1.8e+02
Flux (cm²)
Depth [cm]
0
100
200
300
400
500
600
15
20
25
30
35
40
45
50
55

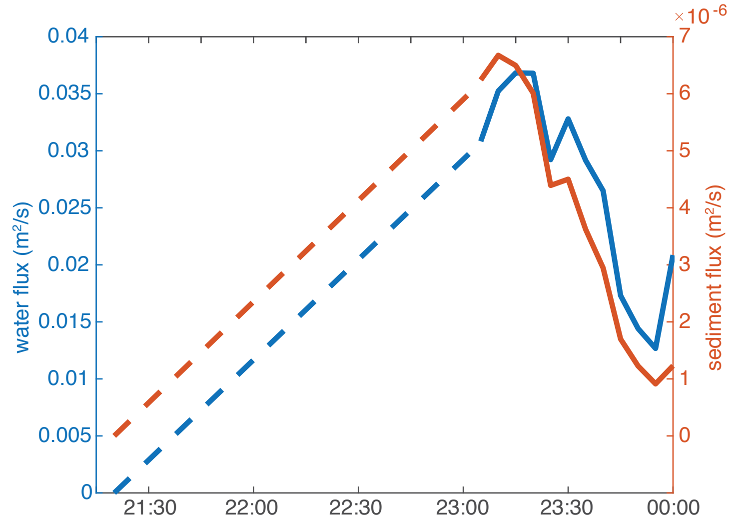
water flux (m²/s)
sediment flux (m²/s)
×10 -6
0
0.005
0.01
0.015
0.02
0.025
0.03
0.035
0.04
0
1
2
3
4
5
6
7
21:30
22:00
22:30
23:00
23:30
00:00

16

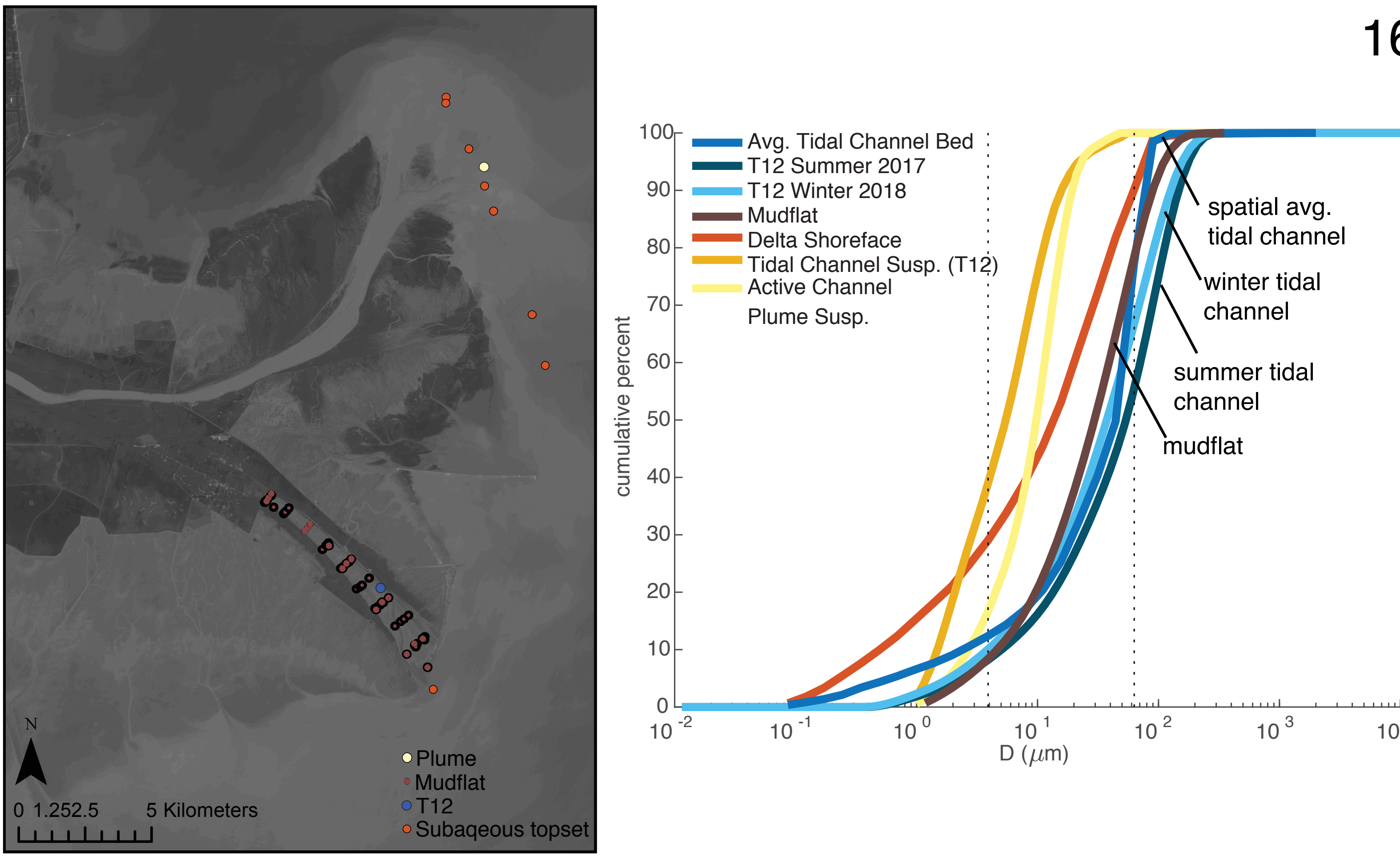

Plume
Mudflat
T12
Subaqeous topset
N
0 1.252.5 5 Kilometers
100
90
80
70
60
50
40
30
20
10
0
cumulative percent
Avg. Tidal Channel Bed
T12 Summer 2017
T12 Winter 2018
Mudflat
Delta Shoreface
Tidal Channel Susp. (T12)
Active Channel
Plume Susp.
spatial avg.
tidal channel
winter tidal
channel
summer tidal
channel
mudflat
10^{-2} 10^{-1} 10^{0} 10^{1} 10^{2} 10^{3} 10^{4}
D (μm)

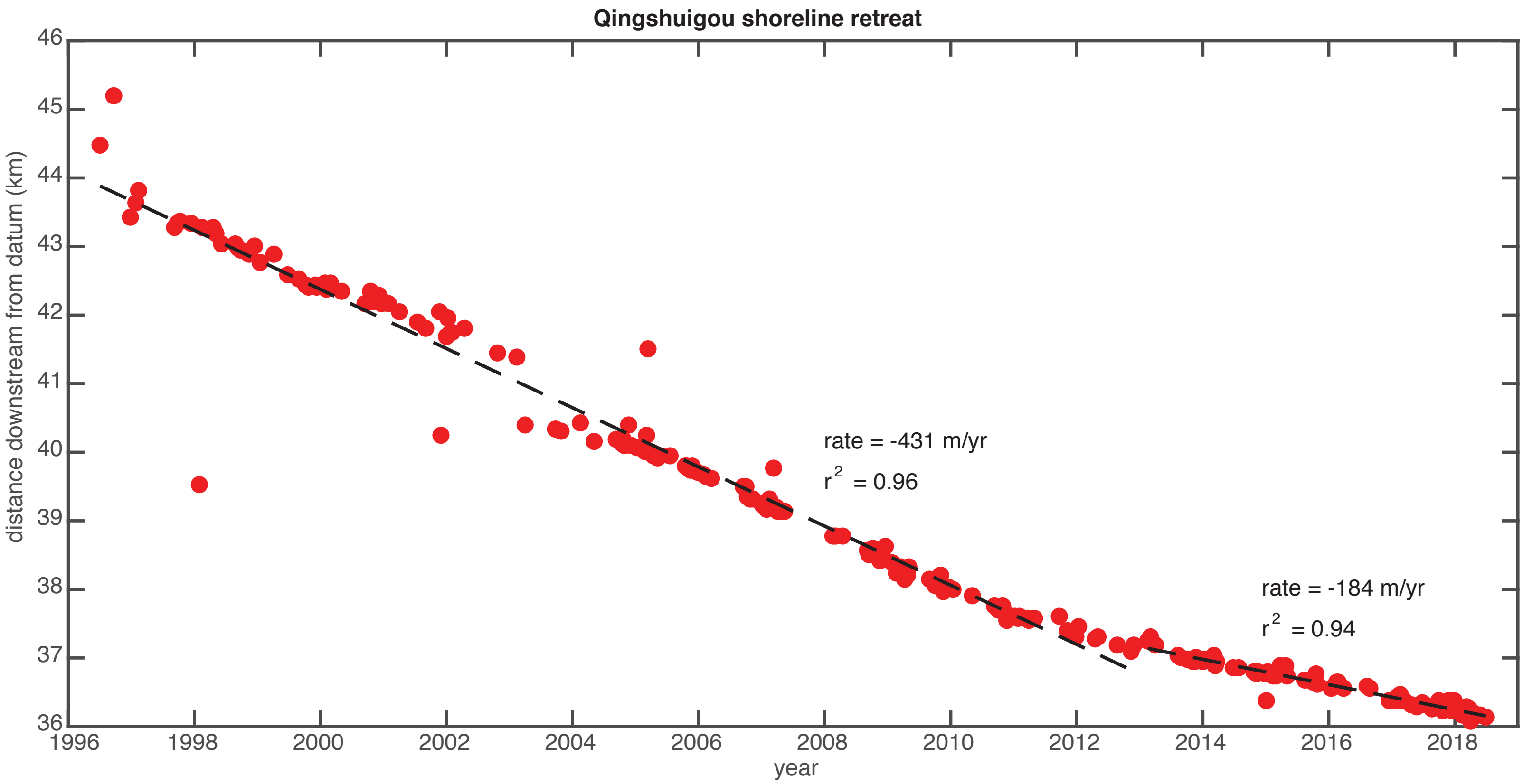

Qingshuigou shoreline retreat
distance downstream from datum (km)
46
45
44
43
42
41
40
39
38
37
36
1996
1998
2000
2002
2004
2006
2008
2010
2012
2014
2016
2018
year
rate = -431 m/yr
r^2 = 0.96
rate = -184 m/yr
r^2 = 0.94

18

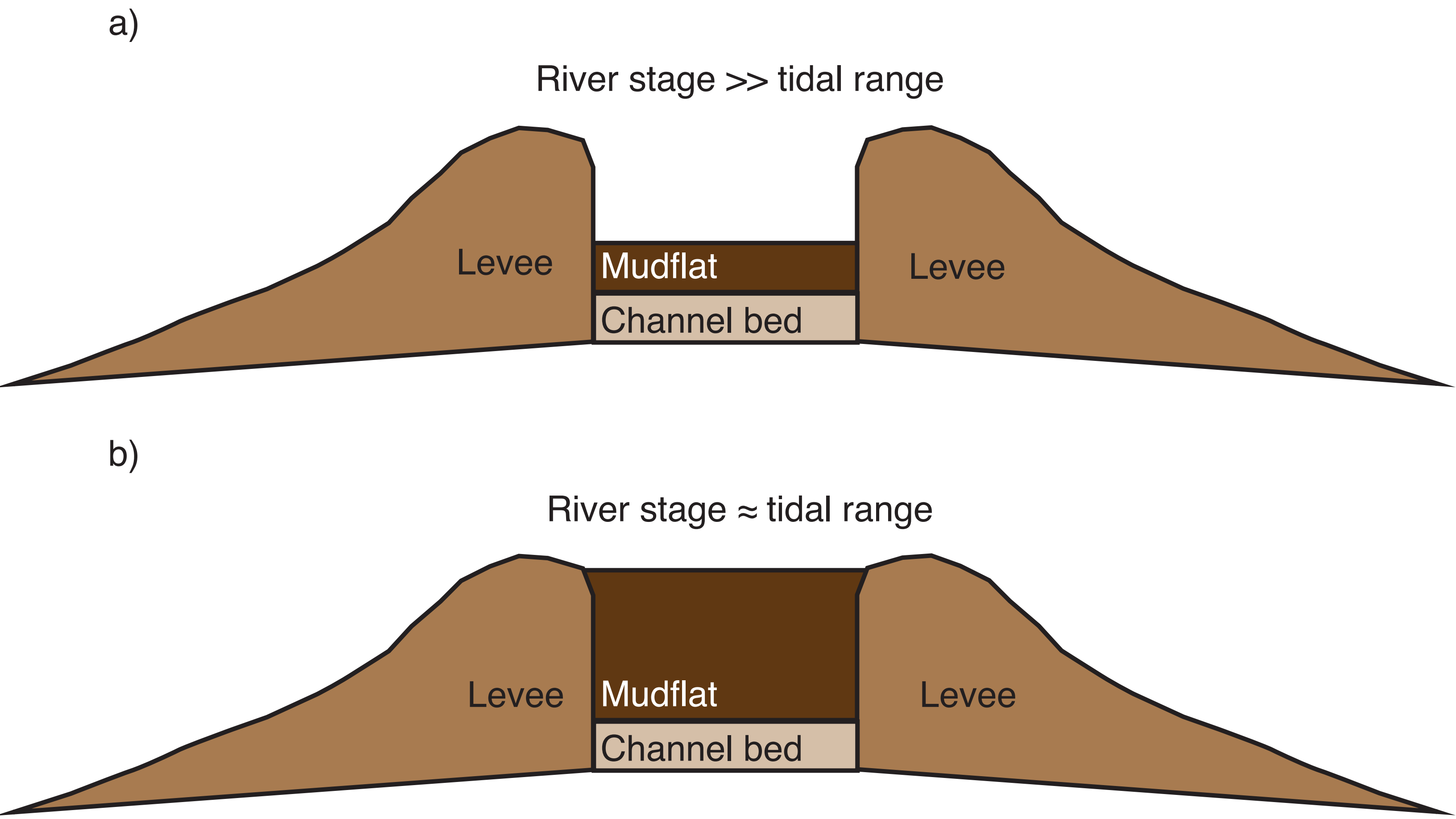
a)
River stage >> tidal range
Levee
Mudflat
Channel bed
Levee
b)
River stage ≈ tidal range
Levee
Mudflat
Channel bed
Levee